



Constrained aerosol forcing for improved climate projections - FORCeS

GA 821205

D1.4 – First parameterizations of key aerosol processes and components

Coordinator:	Stockholm University (SU)
Work package	WP1 - Critical aerosol forcing processes and factors
Lead partners	Foundation for Research and Technology - Hellas (FORTH)
Contributing partners	Forschungszentrum Jülich (FZJ), Barcelona Supercomputing Center (BSC), University of Helsinki (UHEL), University of Eastern Finland (UEF)
Type of document	Report
Dissemination level	Confidential, only for members of the consortium (including the Commission Services)
Due date:	31.03.2021
Submission date:	29.03.2021



This project has received funding from the European Union's Horizon 2020 research and innovation programme under grant agreement No 821205

Document information

Project title:	FORCeS - Constrained aerosol forcing for improved climate projections
Grant Agreement	821205
Coordinators:	Ilona Riipinen (SU) and Annica Ekman (SU)
Project start date:	01.10.2019
Duration of the project:	48 months
Document title:	Deliverable 1.4 – First parameterizations of key aerosol processes and components
Lead author:	Spyros Pandis (FORTH)
Contributing authors:	Alexandra Tsimpidi (FZJ), Vlassis Karydis (FZJ), Thomas Mentel (FZJ), Astrid Kiendler-Scharr (FZJ), Stylianos Kakavas (FORTH), Athanasios Nenes (FORTH/EPFL), Maria Kanakidou (FORTH), Oriol Jorba (BSC), Carlos Perez (BSC), Maria Goncalves (BSC), Tuomo Nieminen (UHEL), Xinyang Li (UHEL), Lubna Dada (UHEL)

History of changes

Version	Date	Authors	Description of Changes

Disclaimer

The contents of this document are the sole responsibility of the authors and do not necessarily reflect the opinion of the European Commission. The European Commission is not responsible for any use that may be made of the information contained in this document.

Copyright © FORCeS Consortium

Table of Contents

1. Summary.....	4
2. Organic Aerosol	4
2.1 Volatility Basis Set Framework	4
2.2 Emissions of LVOCs, SVOCs and IVOCs	5
2.3 Atmospheric Reactions.....	6
2.4 Gas/Aerosol Partitioning	7
2.5 Preliminary Testing and Evaluation of ORACLE-lite.....	8
3. Nitrate Aerosol	9
3.1 ISORROPIA-lite description	11
3.2 ISORROPIA-lite off-line evaluation	12
3.2.1 Computational requirements	12
3.2.2 Evaluation of ISORROPIA-lite against ISORROPIA-II	12
3.3 On-line evaluation of ISORROPIA-lite in PMCAMx	15
3.4 Summary of ISORROPIA-lite testing results.....	18
3.5 Simulation of distribution of condensing nitrates on fine and coarse modes	18
3.6 Nitrates and dust	19
4. Organic and Other Aerosol Absorption	20
4.1 Absorption parameterization in ESMs.....	23
4.2 Proposed BrC implementation in ESMs.....	25
5. Ultrafine Particles	26
5.1 Parameterization of new particle formation and growth rates	26
5.2 Parameterization of sub-grid processing of number emissions.....	27
5.2.1 The sub-grid coagulation parameterization	28
5.2.2 Application of the parameterization in ESMs.....	30
6. References	30

1. Summary

One of the goals of FORCeS is to improve the representation of aerosol processes in ESMs in an effort to increase their accuracy without increasing significantly their computational cost. Based on the results and recommendations of previous EU projects in this research area (EUCAARI, PEGASOS, BACCHUS and ECLIPSE) four key species and processes have been selected. This report describes the first parameterizations developed by FORCeS for the improvement of the simulation of organic aerosol, nitrate aerosol, brown carbon and ultrafine particles in Earth System Models (ESMs). The organic aerosol module is a reduced version (ORACLE-lite) of the Volatility Basis Set-based ORACLE module and describes the volatility distribution of fresh and secondary organic aerosol from anthropogenic and biogenic sources. The aerosol nitrate module includes ISORROPIA-lite, a simplified but also computationally efficient version of the popular ISORROPIA-II aerosol thermodynamic model. ISORROPIA-lite simulates the thermodynamics of the Ca^{2+} - K^{+} - Mg^{2+} - SO_4^{2-} - Na^{+} - NH_4^{+} - NO_3^{-} - Cl^{-} - H_2O system. The nitrate module also includes a parameterization of the partitioning of the nitrate between the fine and coarse particles and a global field of the dust mineralogical composition. The aerosol brown carbon and its corresponding absorption is described with a three-absorbing surrogate species parameterization: one inert primary, one reactive primary that decays with age and one reactive secondary component. Finally, the improvements of the ultrafine particle simulation include a scheme for the parameterization of nucleation and growth to 10 nm and a scheme for the description of sub-grid processing of the fresh primary aerosol number emissions.

2. Organic Aerosol

Despite the explosion in our understanding of organic aerosol processes during the last decade, the advancement of the simulation of the corresponding processes in ESMs has been slow. FORCeS has developed a version of the Volatility Basis Set that is suitable for ESMs. The parameters in this module can be easily updated by the latest laboratory findings about the formation of secondary organic aerosol

The detailed ORACLE module comprehensively describes the Organic Aerosol Composition and Evolution in the atmosphere and has been developed and incorporated in the ECHAM/MESSy Atmospheric Chemistry (EMAC) (Jöckel *et al.*, 2006) by Tsimpidi *et al.* (2014). It is designed to unify all of the technical features required of “state-of-the-science” air quality modules and the latest experimental discoveries that reveal the complex nature of organic aerosol (OA), into a single open-source system that is computationally efficient, flexible, and publicly available. The ORACLE module is based on the volatility basis set framework proposed by Donahue *et al.* (2006). It uses fixed logarithmically-spaced saturation concentration bins to describe the OA volatility distribution and assumes formation of a pseudo-ideal solutions in the organic aerosol phase. This new framework blurs the distinction between the traditional primary (POA) and secondary organic aerosol (SOA), providing a more realistic picture of the behavior of atmospheric organic aerosol. During FORCeS, a reduced-form version (ORACLE-lite) has been developed. The ORACLE-lite module uses a limited number of logarithmically-spaced saturation concentration bins to describe the OA components based on their volatility in order to minimize the computational cost of the module. However, it is still able to accurately simulate the contribution of low volatility (LVOCs), semivolatile (SVOCs) and intermediate volatility organic compounds (IVOCs) from fossil fuel combustion and biomass burning emissions and anthropogenic and biogenic VOCs to the formation of SOA. ORACLE-lite simulates the gas-phase photochemical reactions of SOA precursors, assumes bulk equilibrium between the gas and particulate phases, and distributes the OA in the size modes used by the ESM.

2.1 Volatility Basis Set Framework

The ORACLE-lite module adopts the volatility basis set approach proposed by Donahue *et al.* (2006). It lumps the thousands of organic compounds into groups (surrogate species) with logarithmically-spaced effective saturation concentrations. This framework abandons the traditional distinction between POA and SOA and efficiently treats both semivolatile primary emissions and SOA production, and simulates the chemical evolution of these species under a unified framework. The exact volatility resolution defined and used by ORACLE can be controlled through the interface layer of the module, offering the flexibility to investigate

different schemes. The lite version proposed here includes three surrogate species for POA divided into two groups each with saturation concentrations C^* at 298 K equal to 10^{-2} , 10^1 , 10^4 :

- POA from biofuel combustion, fossil fuel combustion, and other urban sources (fPOA) and
- POA from biomass burning (bbPOA).

The least volatile fraction, at $10^{-2} \mu\text{g m}^{-3}$, describes the low volatility organics in the atmosphere that are mostly in the particulate phase even in remote locations (LV-SOA). The $10 \mu\text{g m}^{-3}$ volatility bin describes the semivolatile organics in the atmosphere which partition between the particle and gas phase at atmospheric conditions (SV-SOA). Finally, even under highly polluted conditions the majority of the material in the $10^4 \mu\text{g m}^{-3}$ volatility bin will exist almost exclusively in the vapor phase (IV-SOA). A similar approach is followed for SOA formed from VOCs. In the lite version of ORACLE, it is assumed that the oxidation of the anthropogenic and biogenic VOC species (aVOCs and bVOCs, respectively) results in two products for each precursor distributed in two volatility bins with effective saturation concentrations at 298 K equal to 1 and $10^3 \mu\text{g m}^{-3}$ at 298 K. A schematic overview of the ORACLE-lite module which include the different aerosol types and chemical processes modeled in the proposed framework is provided in Figure 2.1.

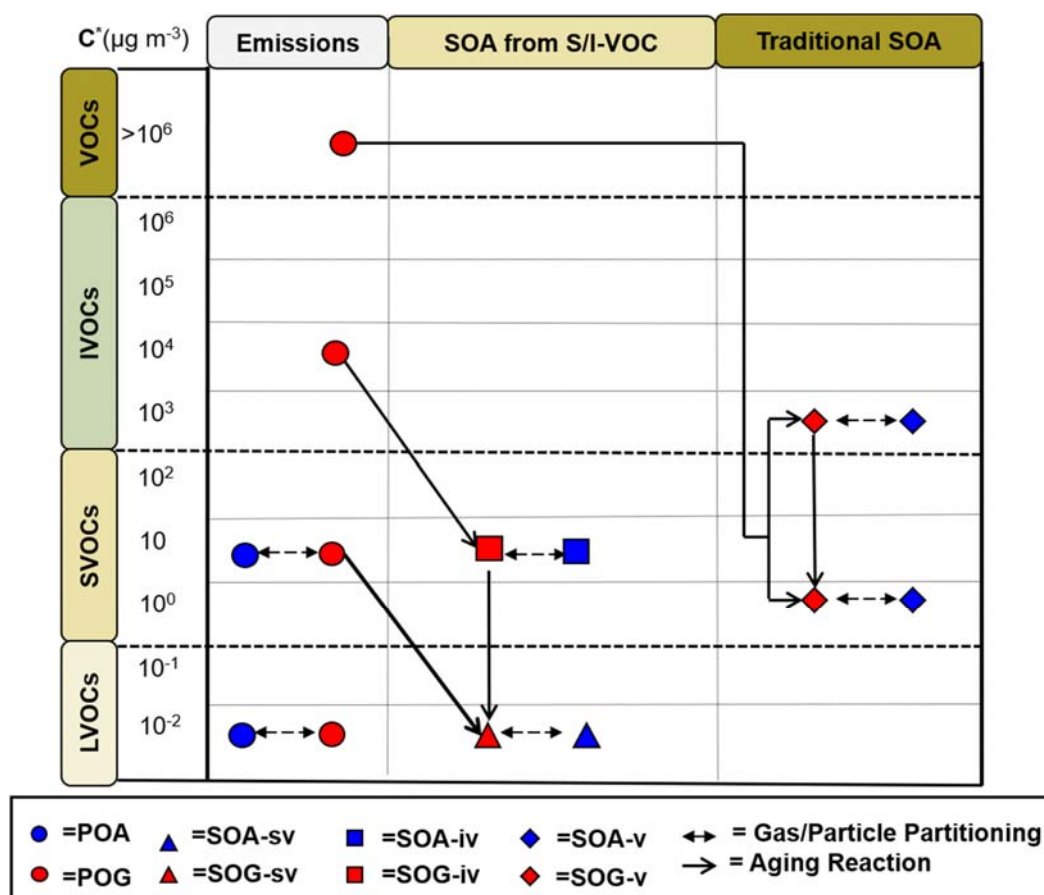


Figure 2.1: Schematic of the VBS resolution and the formation procedure of POA and SOA from LVOCs, SVOCs, IVOCs and VOCs emissions in ORACLE-lite. Red indicates that the compound is in the vapor phase and blue in the particulate phase. The circles correspond to primary organic material that can be emitted either in the gas or in the aerosol phase. The triangles indicate the formation of SOA from SVOCs by fuel combustion and biomass burning sources, while the squares show SOA from IVOCs by fuel combustion and biomass burning sources, and the diamonds the formation of SOA from anthropogenic and biogenic VOC sources. The partitioning processes, the aging reactions and the names of the species used to track all compounds are also shown.

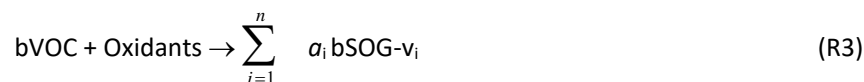
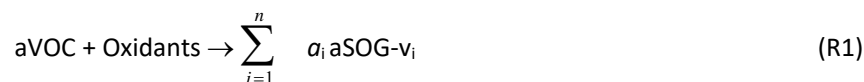
2.2 Emissions of LVOCs, SVOCs and IVOCs

ORACLE-lite distinguishes organic emissions from biomass burning and other combustion sources (biofuel and fossil fuel combustion, and other urban sources) using three surrogate species for each emission category

with effective saturation concentration at 298 K of $C^* = 10^{-2}$, 10^1 , and $10^4 \mu\text{g m}^{-3}$ to cover the volatility range of LVOCs, SVOCs and IVOCs. The emission factors used for the distribution of traditional POA emissions used by current ESMs into these surrogate species are based on the work of Tsimpidi et al. (2016). These emission factors also account for the additional IVOC emissions that are not included in the traditional emission inventories. We assume that the missing IVOC emissions from anthropogenic combustion are 1.5 times the traditional OA emissions included in the inventory; therefore, the sum of the emission factors is 2.5 times the traditional non-volatile POA emissions. No additional IVOC emissions are assumed for open biomass burning and therefore the sum for the biomass burning emission factors is unity. LVOCs and SVOCs are assumed to be emitted as POA, while IVOCs are emitted as primary organic gases (POGs). Then, they are allowed to partition between the gas and particle phase, which can result in some POGs from the evaporation of POA.

2.3 Atmospheric Reactions

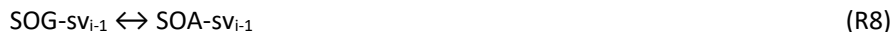
Oxidation of VOCs: The oxidation of VOCs that are considered as SOA precursors is part of the gas-phase chemistry model MECCA. The mechanism considers the oxidation of alkenes, aromatics and isoprene by OH, and the oxidation of olefins and monoterpenes by O_3 , O, OH, and NO_3 . The oxidation products from anthropogenic (alkenes, aromatics, and olefins) and biogenic (monoterpenes and isoprene) VOCs are lumped into two separated secondary organic aerosol (SOA) groups. These groups are further distributed into volatility bins with logarithmically-spaced effective saturation concentrations (Figure 2.1). The photo-oxidation of anthropogenic (aVOCs) and biogenic (bVOCs) is described by the following reactions:



where a_i is the aerosol yield, i is the corresponding volatility bin, and n is the total number of volatility bins. The ORACLE-lite version considers two volatility bins and the corresponding aerosol yields are based on laboratory results from smog-chamber experiments under high- NO_x conditions for aVOCs and low- NO_x conditions for bVOCs (Tsimpidi et al., 2014). This is based on the assumption that urban areas, where most of aVOCs are emitted (~90%), are characterized by high- NO_x conditions (Tsimpidi et al., 2008; Karl et al., 2009) and forested regions by low- NO_x conditions (Pugh et al., 2010; Browne et al., 2013).

Chemical Aging Reactions: ORACLE-lite treats all OA compounds as chemically reactive. However, only homogeneous gas-phase aging is considered since it is rapid compared to heterogeneous reactions with OH (Donahue et al., 2013). In this lite version, the volatilities of the OA surrogate species reacting with OH are reduced by a factor of 10^3 (Figure 2.2) with a rate constant of $0.33 \times 10^{-11} \text{ cm}^3 \text{ molecule}^{-1} \text{ s}^{-1}$ and a 22.5% increase in mass to account for three added oxygen. This represents a more aggressive addition of oxygen and reduction in volatility compared to the standard version of ORACLE but with a reduced reaction rate constant. Existing evidence suggests that the aging of biogenic SOA does not result to an important change in its mass concentration (Ng et al., 2006; Donahue et al., 2012; Murphy et al., 2012) and, therefore, it is assumed here that their chemical aging does not result in a net increase of the corresponding SOA concentration. After the oxidation, anthropogenic SOA reach a final organic matter/organic carbon ratio (OM/OC) of 2.2 (assuming an initial OM/OC of 1.8), which is within the limits (OM/OC:1.8-2.4) of the observed OM/OC of the oxygenated organic aerosols (Aiken et al., 2008). SVOCs and IVOCs can participate in up to two generations of oxidation reaching a final OM/OC up to 1.8 (assuming an initial OM/OC of 1.2), which is also consistent with the observed OM/OC (OM/OC:1.8-2.4) of the oxygenated organic aerosols (Aiken et al., 2008). The chemical aging of SOA is described by the following reactions:





2.4 Gas/Aerosol Partitioning

ORACLE-lite calculates the partitioning of organic compounds between the gas and particle phases by assuming bulk equilibrium and that all organic compounds form a pseudo-ideal solution. The gas/aerosol partitioning is performed in two steps as follows:

Bulk equilibrium: ORACLE-lite calculates the bulk equilibrium gas and aerosol concentrations following the approach of the SOAM-II model of Strader et al. (1999). Considering partitioning of n organic compounds and assuming pseudo-ideal solution, a set of n nonlinear equations is obtained:

$$C_{a,i} = C_{t,i} - x_i c_i^* \text{ for } i = 1, n \quad (\text{E1})$$

$$x_i = \frac{c_{a,i} / M_i}{\sum_{j=1}^n c_{a,j} / M_j} \quad (\text{E2})$$

where $C_{t,i}$ and $C_{a,i}$ are the total and aerosol-phase concentrations of product i in $\mu\text{g m}^{-3}$, respectively, c_i^* is the effective saturation concentration of product i , x_i is the mole fraction of product i in the absorbing organic phase, and M_i is the molecular weight of product i . The molecular weights of all POA, LV-SOA, SV-SOA, and IV-SOA components are assumed to be 250 g mol^{-1} while the molecular weights of bSOA and aSOA are 180 and 150 g mol^{-1} , respectively (Tsimpidi et al., 2014). The temperature dependence of saturation concentrations is described by the Clausius–Clapeyron equation:

$$c_i^* = c_{i,0}^* \frac{T_0}{T} \exp \left[\frac{\Delta H}{R} \left(\frac{1}{T_0} - \frac{1}{T} \right) \right] \quad (\text{E3})$$

where c_i^* and $c_{i,0}^*$ are the saturation concentrations at temperature T and T_0 , respectively, R is the gas constant, and ΔH is the enthalpy of vaporization. In this application an effective ΔH of 30 kJ mol^{-1} is used for all aSOA and bSOA species based on data for α -pinene (Pathak et al., 2007), and a ΔH of 112, 94, 76 is used for the 10^{-2} , 10^1 , $10^4 \mu\text{g m}^{-3}$ volatility bins, respectively, for all organic compounds from fuel combustion and biomass burning sources based on data for large saturated species commonly found in primary emissions (Donahue et al., 2006). ORACLE-lite solves this equation set, which yields the bulk aerosol composition at equilibrium.

Aerosol size distribution: The aerosol size distribution is determined by distributing the change in aerosol mass after the bulk equilibrium into each size mode used by the ESM using a weighting factor (Pandis et al., 1993). Assuming pseudo-ideal solution, the fraction, $f_{i,k}$, of total flux of species i between gas and aerosol phases that condenses onto or evaporates from an aerosol mode k is given by:

$$f_{i,k} = \frac{N_k d_k (c_i - x_{i,k} c_i^*) / (\beta_k + 1)}{\sum_{l=1}^m N_l d_l (c_i - x_{i,l} c_i^*) / (\beta_l + 1)} \quad (\text{E4})$$

where N_k and d_k are the number and mean diameter of particles in the mode k , respectively, m is the total number of aerosol modes, $\beta_k = 2\lambda / \alpha d_k$, α is the aerosol accommodation coefficient, and λ is the mean free path of air molecules (Pandis et al., 1993). The above equation is solved iteratively at each time step and

determines the OA composition of each mode. Overall, the user is allowed to use up to 3 hydrophilic modes (Aitken, accumulation, coarse) for the size distribution of all OA surrogate species. The ORACLE-lite version can also be applied with only the accumulation mode to further limit the computational cost of the module. It can also be used easily with ESMs using a sectional approach for the description of the aerosol size distribution.

2.5 Preliminary Testing and Evaluation of ORACLE-lite

For testing purposes, the ORACLE-lite has been added to the EMAC chemistry-climate model (CCM) with a spectral resolution of T63L31, corresponding to a horizontal grid resolution of approximately $1.9^\circ \times 1.9^\circ$ and 31 vertical layers extending to 25 km. EMAC was used to simulate 10 years covering the period 2000-2009 and the first year was used as spin-up. Figure 2.2 depicts the simulated, decadal average global surface concentrations of total OA, POA, SOA from SVOCs and IVOCs, and SOA from the oxidation of the traditional VOCs. High OA concentrations are predicted over regions affected by biomass burning and biogenic VOC emissions: tropical forests and savannas of South America (Amazon Basin), Africa (Congo Basin), and Southeast Asia. Considerable OA concentrations are also predicted over the industrialized regions of the Northern Hemisphere (i.e., China, Europe, and Eastern US), where strong fossil and biofuel combustion-related sources are located. The model predicts a continental background OA concentration of around $2 \mu\text{g m}^{-3}$, which is mainly due to the condensation of oxidized low volatility organic vapors. These compounds are formed from the reactions of VOCs, IVOCs and SVOCs, which have been emitted in the gas phase and have been efficiently transported some distance from their sources. The effects of trade wind transport of biomass burning OA off the subtropical west coasts of Africa and America are discernible in Figure 2.2a. In these regions, the OA concentration is increased by long-range transport of continental air masses to adjacent ocean areas.

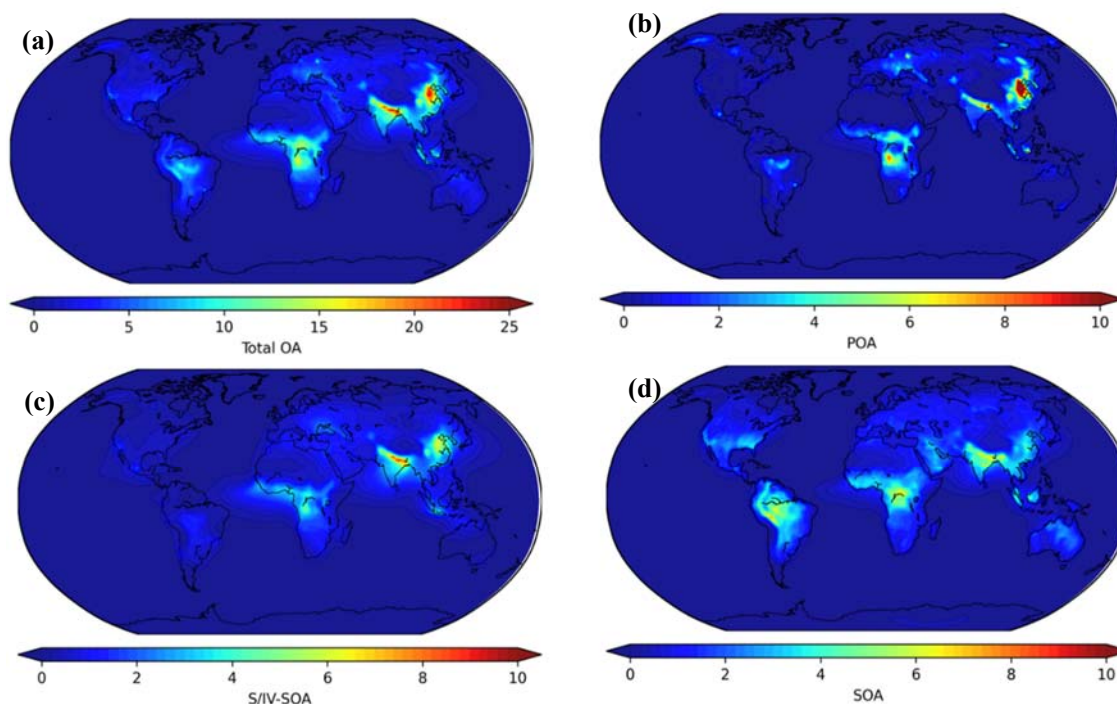


Figure 2.2: Predicted decadal average surface concentrations (in $\mu\text{g m}^{-3}$) of (a) total OA (b) POA from fuel combustion and biomass burning emissions (c) SOA from the oxidation of SVOCs and IVOCs from fuel combustion and biomass burning emissions and (d) SOA from the oxidation of anthropogenic and biogenic VOC emissions during the years 2000-2009. This is the first test of ORACLE-lite in EMAC.

Higher POA concentrations ($\sim 10 \mu\text{g m}^{-3}$) are predicted over densely populated and industrialized areas (e.g., Eastern China, Northern India, Eastern Europe, etc.), where there are substantial anthropogenic combustion emissions, and over the tropical rainforests (i.e., Amazon, Congo, and Southeast Asia) and the boreal forests

(i.e., Alaska, Canada, and Russia) due to substantial emissions from forest and savannah fires. Downwind of the sources, POA concentrations decrease substantially since they are diluted and a large fraction is predicted to evaporate during transport. This results in a highly inhomogeneous spatial distribution of POA concentrations (Figure 2a). In contrast, S/IV-SOA is more regionally distributed with high concentrations (up to $7 \mu\text{g m}^{-3}$) downwind of the anthropogenic and biomass burning sources due to its continuous production and long-range transport from SVOCs and IVOCs (Figure 2b). This results in a continental S/IV-SOA background of $\sim 1 \mu\text{g m}^{-3}$ and in concentrations of around $2 \mu\text{g m}^{-3}$ over marine regions close to anthropogenic sources (e.g., Arabian Sea, Yellow Sea) and over the South Atlantic Ocean which is strongly influenced by long-range transport of biomass burning from the Congo Basin.

SOA-v formed from the oxidation of biogenic and anthropogenic VOCs also contribute significantly to SOA formation, especially considering the aging reactions of anthropogenic SOA-v. ORACLE-lite calculates highest SOA-v concentrations over the Amazon Basin rainforest ($\sim 6 \mu\text{g m}^{-3}$) mostly due to the oxidation of isoprene. Over the Congo Basin rainforest, where isoprene emissions are similar to monoterpene emissions, the SOA-v average surface concentration is $3\text{--}5 \mu\text{g m}^{-3}$. Photochemical aging adds significantly to anthropogenic SOA-v resulting in a wider distribution of SOA-v around the more polluted regions of the Northern Hemisphere and in the vicinity of urban areas. The highest concentrations occur over India and Bangladesh (up to $7 \mu\text{g m}^{-3}$). Over Europe, the predicted SOA-v concentrations are up to $2 \mu\text{g m}^{-3}$. Over the US SOA-v concentrations are relatively high over California and the southeastern USA (up to $4 \mu\text{g m}^{-3}$).

Figure 2.3 shows a comparison of predicted OA concentrations by EMAC using ORACLE-lite with measurements from the European Monitoring and Evaluation Programme (EMEP) and the Interagency Monitoring of Protected Visual Environments (IMPROVE) networks as well as short-term measurement data collected over East Asia as summarized by Jo et al. (2013).

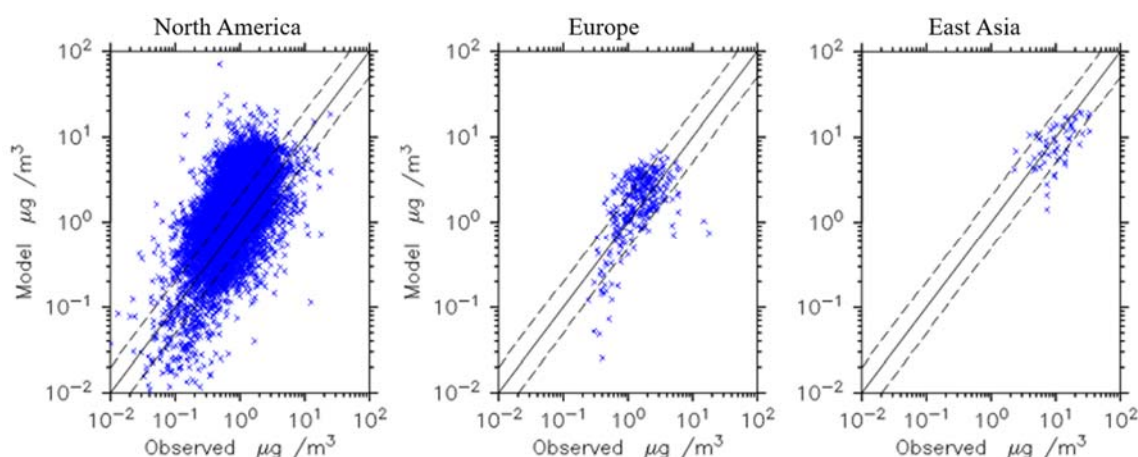


Figure 2.3: Scatter plot comparing model predictions of total OA concentration (in $\mu\text{g m}^{-3}$) with observations from the (a) IMPROVE network in the United States, (b) EMEP network in Europe and East Asian sites from 2000 to 2009. Each point represents a monthly average value. Also shown the 1:1, 2:1 and 1:2 lines.

Each point of the scatter plots represents a monthly average value at a particular monitoring station. The model, despite its coarse resolution, captures the monthly average concentrations of OA over the USA, Europe, and Asia relatively well. This is rather encouraging given the expected uncertainties in the emission inventory and in a number of parameters used by the model such as the emission fractions for POA from fuel combustion and biomass burning, the reaction rates and aerosol yields that accompany the formation of SOA from SVOCs, IVOCs and VOCs, etc. However, despite these limitations, the modelled total OA concentrations are generally in reasonable agreement with the measurements.

3. Nitrate Aerosol

Even if our understanding of the formation of inorganic nitrate salts has advanced and the corresponding processes are reasonably well simulated in regional CTMs, the computational cost has seriously limited and

in most cases prohibited the simulation of this important aerosol component and its corresponding forcing. In FORCeS we have explored ways to reduce the computational cost of the simulation of the following processes: formation and evaporation of ammonium nitrate, reactions of nitric acid with coarse sea-salt and dust particles, and the competition of fine and coarse particles for the available nitric acid. This has resulted in the development of ISORROPIA-lite, a computationally efficient atmospheric aerosol thermodynamics module that can be used by ESMs with a small additional computational cost to simulate aerosol nitrates.

Atmospheric particulate matter (PM) is composed of inorganic salts, organic compounds and elemental carbon, oxides of trace metals, crustal material and water. Inorganic salts often constitute 50% or more of fine particulate matter (particles with diameter less than 2.5 μm) with sulfate (SO_4^{2-}), bisulfate (HSO_4^-), ammonium (NH_4^+), nitrate (NO_3^-), chloride (Cl^-) and sodium (Na^+) ions being the dominant ones (Heitzenberg, 1989; Fountoukis and Nenes, 2007). These inorganic salts are responsible for most of the water uptake by fine PM and therefore for a large fraction of the interactions between aerosols and atmospheric radiation (Burgos et al., 2019). Dust components such as Ca^{2+} , and Mg^{2+} together with hygroscopic sea salt (Na^+ , Cl^-) are found mainly in the coarse PM fraction. These aerosols can exist in solid and/or liquid form depending on the ambient relative humidity. Computing the phase state and composition of aerosols in thermodynamic equilibrium is a complex computational problem, because it involves the solution of a system of several of nonlinear algebraic equations (Nenes et al., 1999). This thermodynamic calculation needs to be repeated billions of times (or more) in a chemical transport model and therefore contributes a lot to the computational cost of the model. While these thermodynamic modules are standard in all regional chemical transport models, they are not included in a lot of the Earth System Models. For example, EC-Earth (Hazeleger et al., 2011) and ECHAM5 (Roeckner et al., 2003) do not simulate aerosol thermodynamics, while NorESM (Bentsen et al., 2013; Iversen et al., 2013) uses a zeroth-order estimate for aerosol nitrate formation (Kirkevåg et al., 2013).

Several thermodynamic equilibrium models have been developed during the last forty years treating different sets of aerosol components and using different thermodynamic and numerical approaches. AIM2 (Wexler and Clegg, 2002), SCAPE2 (Kim et al., 1993a, b; Kim and Seinfeld, 1995; Meng et al., 1995), GFEMN (Ansari and Pandis, 1999a, b), EQSAM (Metzger et al., 2002a, b, 2006, 2016; Metzger and Lelieveld, 2007), EQUISOLV II (Jacobson et al., 1996; Jacobson, 1999a, b), ISORROPIA (Nenes et al., 1998), ISORROPIA-II (Fountoukis and Nenes, 2007) are some examples. One of the challenges faced by these aerosol thermodynamic models is that inorganic atmospheric aerosol tends to be an aqueous solution at high RH, can be dry solid at low enough RH, and in intermediate RH conditions it can be either solid or an aqueous solution or both. Previous studies have shown that assuming that the particles do not include water at RH below their deliquescence point (this is their stable state) results in higher concentrations of nitrate and ammonium (mainly in NH_4NO_3 and $(\text{NH}_4)_2\text{SO}_4$ form) compared to assuming a metastable state for ambient $\text{RH} < 50\%$ (Ansari and Pandis, 2000; Moya et al., 2007; Fountoukis et al., 2009). At mid-range RH region (50–60%) metastable nitrate concentrations are higher (Ansari and Pandis, 2000), while for higher RHs ($> 60\%$) solids dissolve and stable and metastable state predictions become identical. Karydis et al. (2016) using the EMAC global model found that the tropospheric burden of nitrate aerosol decreases marginally by just 2% assuming metastable aerosol. Furthermore, according to a recent study (Burgos et al., 2020) earth system models tend to overpredict particle light scattering and hygroscopicity parameterizations in the lower RH range may be responsible for this error.

Assuming a metastable equilibrium state across the entire RH range, as it is expected, leads to higher concentrations of aerosol water than a stable state affecting the size, lifetime and scattering efficiency of particles (Bougiatioti et al., 2016). Organic aerosol could also contribute significantly to the total aerosol water although it is less hydroscopic than inorganic salts (Guo et al., 2015; Bougiatioti et al., 2016; Jathar et al., 2016; Jin et al., 2020). It has been shown that the hygroscopicity parameter k of the organic species ranges between 0.01 and 0.5 (Petters and Kreidenweis, 2007). Therefore, including organic aerosol water in inorganic aerosol thermodynamics could lead to secondary inorganic aerosol formation since the aqueous surface of particles for gas uptake increases (Seinfeld and Pandis, 2006; Guo et al., 2015).

Computational time is another important factor. The first generation of aerosol thermodynamics modules was developed with accuracy as their major objective and little attention was paid to computational efficiency. For example, Fountoukis and Nenes (2007) have shown that ISORROPIA-II is more than one order

of magnitude faster than SCAPE2. Most of the large scale aerosol transport models (CMAQ, PMCAMx, GEOS-Chem, EMAC, etc.) use ISORROPIA-II for the comprehensive simulation of inorganic aerosol thermodynamics because of its computational efficiency. ISORROPIA is actually faster than ISORROPIA-II, because it does not simulate the thermodynamics of crustal species (Ca, K, Mg). Treating crustal species as equivalent sodium introduced significant errors and is not a good solution (San Martini et al., 2005). ISORROPIA-II in its default mode treats the aerosol as solid (stable) at low RH, and both solid and liquid at intermediate RH. It also calculates the binary activity coefficients from the corresponding equations (Bromley, 1973; Kusik and Meissner, 1978; Fountoukis and Nenes, 2007) every time that they are needed in the various iterations of its algorithms. EQSAM4clim (Metzger et al., 2016) is a thermodynamic model developed for climate simulations. It is based on a hygroscopic growth parameterization accounting for aerosol water uptake from the deliquescence RH up to supersaturation, eliminating the need for iterations. Koo et al. (2020) using EQSAM4clim instead of the default mode of ISORROPIA in CAMx reduced the computational time by 4% during winter and 7% during summer.

Despite the previous efforts to produce both accurate and computationally efficient aerosol thermodynamics modules, additional improvements are needed to make them suitable for the computationally demanding long simulations of ESMs. In this work we test the hypothesis that simplifications of the treatment of the inorganic aerosol state and the activity coefficients can accelerate the calculations introducing only small discrepancies. Therefore, a more computationally efficient version of ISORROPIA-II, ISORROPIA-lite is presented. This new module solves only the metastable state problem and always uses the pre-calculated tables of binary activity coefficients in order to save computational time. The predictions of ISORROPIA-lite are first compared against the predictions of ISORROPIA-II (stable state solution) without the organic aerosol water effects off-line and in the chemical transport model PMCAMx, in terms of composition and computational requirements.

3.1 ISORROPIA-lite description

ISORROPIA-II version 2.3, which is the current version of the module (Fountoukis and Nenes, 2007) is used as the starting point in this work. Earlier versions of ISORROPIA-II did not consider properly the partitioning of NH_3 between the aqueous and gas phases under all possible conditions resulting in neutral particles (pH around 7) too often (Song et al., 2018). This issue affected the forward mode pH calculations and has been resolved in version 2.3. The baseline ISORROPIA-II model used in this study calculates explicitly the activation coefficients of mixtures and also assumes that the aerosol is always in a stable state, therefore it is solid at RH below the mutual deliquescence RH of its components. The module is tested in the partitioning mode.

ISORROPIA-lite is a lighter and more computationally efficient version of ISORROPIA-II (Fountoukis and Nenes, 2007). Compared to ISORROPIA-II, it treats the thermodynamics of Ca^{2+} - K^+ - Mg^{2+} - SO_4^{2-} - Na^+ - NH_4^+ - NO_3^- - Cl^- - H_2O aerosol systems. Two modifications have been made to the thermodynamic equilibrium model ISORROPIA-II to develop the new module. ISORROPIA-lite assumes that the aerosol exists as an aqueous solution (metastable state) even at low RH. The routines related with the stable state solution (solid+liquid aerosol) have been removed. The second modification has to do with the calculation of the activity coefficients. In the default version of ISORROPIA-II, the activity coefficients are computed during the runtime of the model combining the Kusik and Meissner (1978) model for specific ionic pairs with the Bromley's (1973) activity coefficients mixing rule for multicomponent mixtures. In ISORROPIA-lite tabulated Kusik-Meissner binary activity coefficient data for each salt is used. Therefore, an internal database is queried every time these activity coefficients are needed.

The system modeled by ISORROPIA-lite consists of exactly the same components as ISORROPIA-II in the gas phase (Fountoukis and Nenes, 2007). The same applies for the aqueous phase, but the new module can also calculate the water content of each salt contained in particles together with organic aerosol water. This makes the change of the corresponding modules in chemical transport models trivial. The only solid salt that is allowed to form in ISORROPIA-lite is calcium sulfate (CaSO_4) which is considered completely insoluble. The rest of the salts are assumed to dissolve because of the metastable state assumption.

As in ISORROPIA and ISORROPIA-II, ISORROPIA-lite can be used to solve either the partitioning (forward) problem or estimate the water content and pH of the particles together with the corresponding equilibrium

vapor concentrations (reverse problem). In the partitioning problem the known quantities are RH, temperature (T), the organic aerosol concentration, the organic aerosol hygroscopicity parameter κ , the organic aerosol density and the total (gas+aerosol) concentrations of ammonia, sulfuric acid, sodium, hydrochloric acid, nitric acid, calcium, potassium, and magnesium. In the reverse problem the only difference is that only the aerosol concentrations of ammonium, chloride, and nitrate are known (together with sulfate, sodium, calcium, potassium, and magnesium that reside only in the particulate phase). In both cases the appropriate set of equilibrium equations are solved together with electroneutrality, water activity equations and mass conservation in order to compute the concentrations of species at thermodynamic equilibrium. More information about the thermodynamic properties of the modeled species, the equilibrium reactions and constants and the thermodynamic equilibrium calculations of inorganic species can be found in Fountoukis and Nenes (2007).

3.2 ISORROPIA-lite off-line evaluation

3.2.1 Computational requirements

ISORROPIA-lite was first evaluated off-line against the default ISORROPIA-II for a standard set of conditions covering the full range of tropospheric conditions. All the timing tests were performed on a computer with two Intel Xeon Silver 4110 CPU 2.1 GHz and 64 GB of RAM. The default ISORROPIA-II version required 6.5 CPU s, 52% more than the 4.2 CPU s required by ISORROPIA-lite. Therefore, replacing ISORROPIA-II by ISORROPIA-lite, for these tests at least will result in a reduction of the corresponding computational cost by approximately 35%. We also run this suite of tests with a version of ISORROPIA-lite using the complete activity calculation module. The reduction of the CPU time due to the assumption of metastable aerosol was 9%. The look-up tables of the activity coefficients were the major contributor (another 26%).

In a second off-line test we used the predictions of PMCAMx only at the ground level (European conditions) for the simulation of May 2008 (23,680 in total) as inputs for the default ISORROPIA-II and ISORROPIA-lite. These suites of predictions are included in the standard set of conditions but they are also studied separately because of their importance for air quality and radiative forcing. For this test ISORROPIA-II required 55% more CPU time than ISORROPIA-lite (0.42 versus 0.27 s). The acceleration of the calculations by ISORROPIA-lite was the same as the first test and equal to 35% of the time required by ISORROPIA-II. We quantified the reasons for this improvement with versions of ISORROPIA-lite using full activity calculations or assuming stable aerosol. The use of the look-up tables of the activity coefficients reduced the CPU time by 18% of the default ISORROPIA-II and the simplification of the metastable state contributed another 17%.

Differences in the frequency of occurrence of conditions suitable for the formation of a stable aerosol state (solid+liquid particles) but also for the activity coefficients calculation at lower temperatures are responsible for small differences in performance of ISORROPIA-lite. The higher the frequency the higher the computational savings offered by the new module. Calculating organic aerosol water did not affect the computational speed.

3.2.2 Evaluation of ISORROPIA-lite against ISORROPIA-II

The predictions of ISORROPIA-lite were first compared with those of the default ISORROPIA-II model for both off-line tests. We use as metrics for the evaluation the normalized mean bias (NMB) and the normalized mean error (NME), defined as:

$$\text{NMB} = \frac{\sum_i^n [\text{ISORROPIA-lite}_i - \text{ISORROPIA-II}_i]}{\sum_i^n \text{ISORROPIA-II}_i}, \quad \text{NME} = \frac{\sum_i^n |\text{ISORROPIA-lite}_i - \text{ISORROPIA-II}_i|}{\sum_i^n \text{ISORROPIA-II}_i}$$

where ISORROPIA-lite_i and ISORROPIA-II_i are the corresponding predictions of each model and n is the total number of test cases examined.

The discrepancies between the ISORROPIA-lite and ISORROPIA-II predictions for the concentrations of the various semivolatile aerosol components are all less than 25% (Table 3.1). They are lower for chloride, a little more for ammonium and higher for nitrate and water. For the gas phase components, they are also less than 25%. For ammonia and hydrochloric acid, they are 10% or less and for nitric acid they are higher. These discrepancies are mainly found at low to intermediate RHs, especially when a particle contains both solid and

liquid phase according to ISORROPIA-II, due to the assumed metastable state in ISORROPIA-lite. Please note that for a lot of these conditions the metastable state may be correct, so these discrepancies should not be viewed as errors of ISORROPIA-lite.

Table 3.1: Normalized mean biases and errors for the off-line tests of ISORROPIA-lite.

	NH ₄ ⁺	Cl ⁻	H ⁺	NO ₃ ⁻	HNO ₃ (g)	HCl (g)	NH ₃ (g)	H ₂ O	Dry PM
ISORROPIA-lite versus default ISORROPIA-II									
<i>Standard set of conditions</i>									
NMB (%)	7.8	8.4	135	23.7	-22.3	-6.2	-10.7	41.7	4.5
NME (%)	8.2	10.2	137	23.9	22.5	7.5	11.3	41.8	4.7
<i>European ground conditions</i>									
NMB (%)	7.7	3.8	64	12.8	-20.9	-4.3	-5.5	13.4	3.1
NME (%)	8.2	4.2	68	13.2	21.5	4.7	5.8	13.6	3.2
Pre-calculated tables ISORROPIA-II versus default ISORROPIA-II									
<i>Standard set of conditions</i>									
NMB (%)	-0.2	-0.4	1.4	-0.4	0.4	0.3	0.3	-1.5	-0.1
NME (%)	1.4	1.2	11.7	4.4	4.2	0.9	1.9	2.3	0.8
<i>European ground conditions</i>									
NMB (%)	-1.6	-0.9	-3.6	-2.5	4.1	1	1.2	-2.1	-0.6
NME (%)	2.5	1.3	9.2	4.1	6.6	1.4	1.8	2.4	1
Metastable state ISORROPIA-II versus default ISORROPIA-II									
<i>Standard set of conditions</i>									
NMB (%)	7.9	8.6	136	23.7	-22.3	-6.4	-10.8	41.7	4.5
NME (%)	8.1	9.9	137	23.7	22.3	7.3	11.2	41.7	4.6
<i>European ground conditions</i>									
NMB (%)	8.7	4.1	65	14.7	-24	-4.6	-6.2	13.5	3.5
NME (%)	8.7	4.1	65	14.7	24	4.6	6.2	13.5	3.5
ISORROPIA-lite versus default ISORROPIA-II (water presence)									
<i>Standard set of conditions</i>									
NMB (%)	9.1	9.3	77	22.7	-24.4	-7.4	-12.8	34.9	5.1
NME (%)	9.3	9.8	79	22.8	24.6	7.9	13.1	35	5.2
<i>European ground conditions</i>									
NMB (%)	8.4	3.8	30	12.7	-23.4	-4.5	-6	12.3	3.3
NME (%)	8.9	4.2	34	13	24	5	6.4	12.5	3.4

For both set of conditions, ISORROPIA-lite in general tends to predict higher amounts of inorganic aerosol and lower concentrations of inorganic gases than ISORROPIA-II (Fig. 3.1).

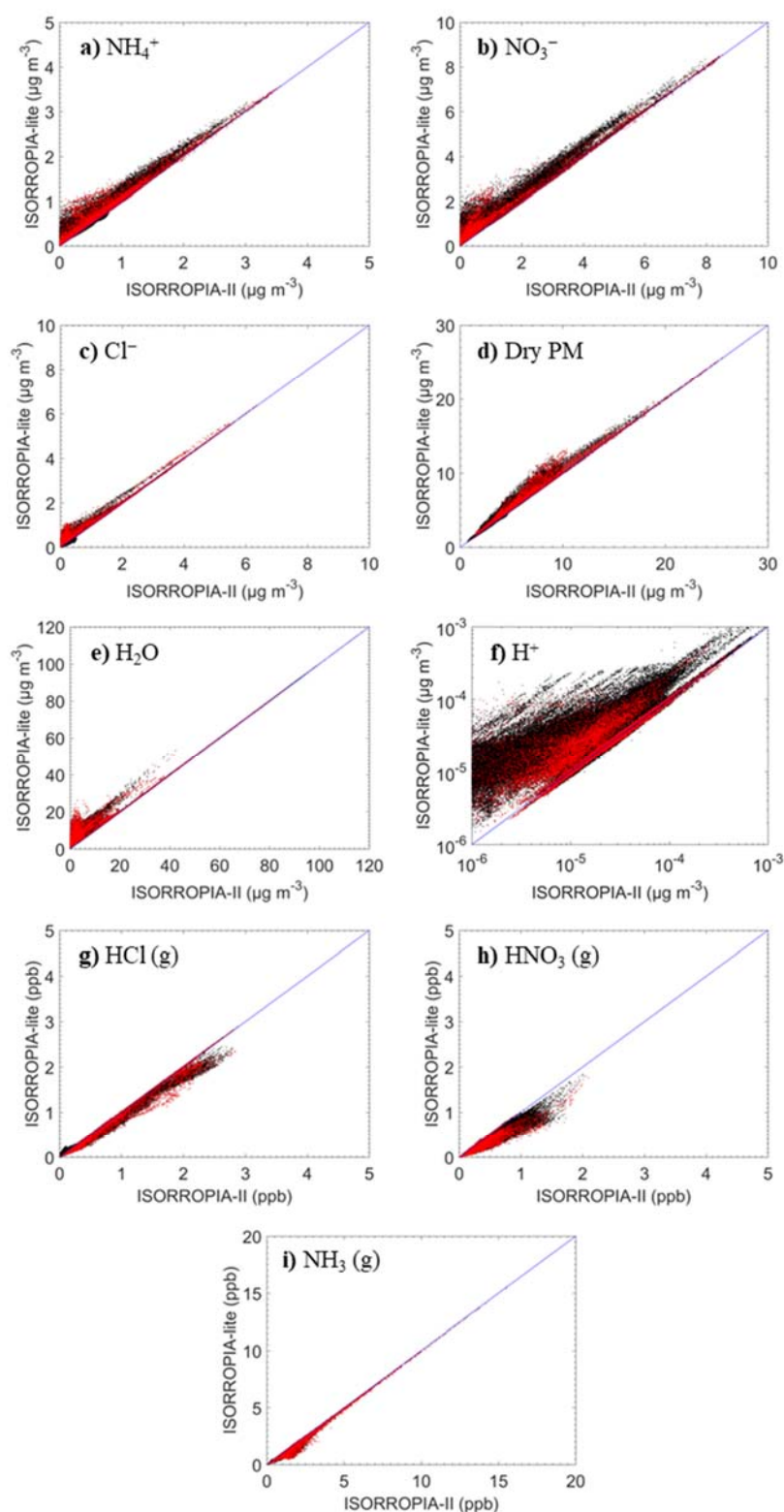


Figure 3.1. Comparison of the particulate and gas-phase concentrations predicted by ISORROPIA-II and ISORROPIA-lite for the off-line simulations for the standard (black) and European (red) set of conditions: **a)** ammonium, **b)** nitrate, **c)** chloride, **d)** dry PM, **e)** water, **f)** hydrogen ion, **g)** hydrochloric acid, **h)** nitric acid, and **i)** ammonia. There are 331,520 points in these graphs.

The mean errors are small and range from 4% for chloride to 23% for nitrate. For water, the mean error was 42% for the standard set of conditions and 14% for the European. The highest discrepancies are found for the hydrogen ion (H^+) predictions (137% for the standard set, 68% for the European set).

The effect of the two changes, activity coefficient calculations and metastable state assumptions, on the predictions of ISORROPIA-II and the discrepancies with ISORROPIA-lite can be quantified examining the results of the corresponding tests in which only one of the two changes was made. The introduction of the pre-calculated tables has a small effect on the ISORROPIA-II predictions for both sets of conditions with mean errors varying from 1.2% for chloride to 6.6% for nitric acid (Table 3.1). Even for the H^+ concentration the mean error is equal to 12% for the standard set and 9% for the European conditions. This concentration differences corresponds to up to 0.2 pH units. The simplification leads to slightly lower predicted concentrations with biases less than 3% for all the major aerosol components and water and slightly higher concentrations (biases less than 4%) for all the inorganic gases. These results strongly suggest that pre-calculated tables introduce small errors in both sets of conditions; therefore, they represent a relatively safe simplification in order to speed up the calculations.

The assumption of the metastable state at all RH conditions had, as expected from the discussion so far, the highest impact on the ISORROPIA-II predictions. The comparison of a version of ISORROPIA-II assuming metastable state (and using the complete activation coefficient module) with the default version of ISORROPIA-II was used for the analysis. For both set of conditions, the normalized mean errors range from 4.1% for chloride to 24% for nitric acid (Table 3.1). Water mean error was equal to 41.7% for the standard set of conditions and 13.5% for the European. The highest discrepancy (137% for the standard set, 65% for the European set) was found for H^+ . Therefore, the assumed metastable equilibrium state is mainly responsible for the discrepancies of the predictions of the two thermodynamic modules.

The upper levels of the atmosphere, included in the standard set of conditions, are characterized by lower RHs and temperatures than the ground level. Therefore, frequency of conditions suitable for the formation of a stable aerosol state (solid+liquid particles), which increase with altitude, are responsible for the error increases in the standard set of conditions. Nevertheless, in both set of conditions the greatest discrepancies were found in water and hydrogen ion levels, because the stable state solution of ISORROPIA-II at low RHs predicts solid aerosol where H^+ and water do not exist (were set equal to zero for the comparison), while ISORROPIA-lite always predicts an aqueous solution. This leads to PM pH predictions by ISORROPIA-lite up to 2 units (acidic), while the default ISORROPIA-II does not predict pH in such cases.

We also compared the predictions of ISORROPIA-lite with those of the default ISORROPIA-II model only when an aqueous phase was also predicted by ISORROPIA-II (water presence). Approximately 75% of the standard set of conditions and 83% of the European were such cases. For both sets of conditions, the discrepancies between the ISORROPIA-lite and ISORROPIA-II predictions for the concentrations of the various aerosol components and gases were all again less than 25% (Table 3.1). For water, the mean error was 35% for the standard set of conditions and 12.5% for the European. As expected, for the hydrogen ion (H^+) predictions the errors were lower (79% for the standard set, 34% for the European set). These concentration differences correspond to less than 0.3 pH units. Therefore, the major differences in the predictions of the two modules for the levels of atmospheric inorganic PM are expected when a particle, according to ISORROPIA-II, consists of both solid and liquid phases, which happens at low to intermediate RHs.

3.3 On-line evaluation of ISORROPIA-lite in PMCAMx

ISORROPIA-lite was added to the three-dimensional regional chemical transport model PMCAMx replacing ISORROPIA-II. The model was then applied over Europe during May 2008, which is the EUCAARI summer intensive measurement period. The modeling domain, including all of Europe, is a region of $5400 \times 5832 \text{ km}^2$. The grid resolution used is $36 \times 36 \text{ km}$ (24,300 cells per layer) and there are 14 vertical layers with the total height extending up to 6 km above ground level. The predicted ground level concentrations of the major inorganic PM components by PMCAMx using the default version of ISORROPIA-II and the corresponding changes when ISORROPIA-lite is used are shown in Fig. 3.2.

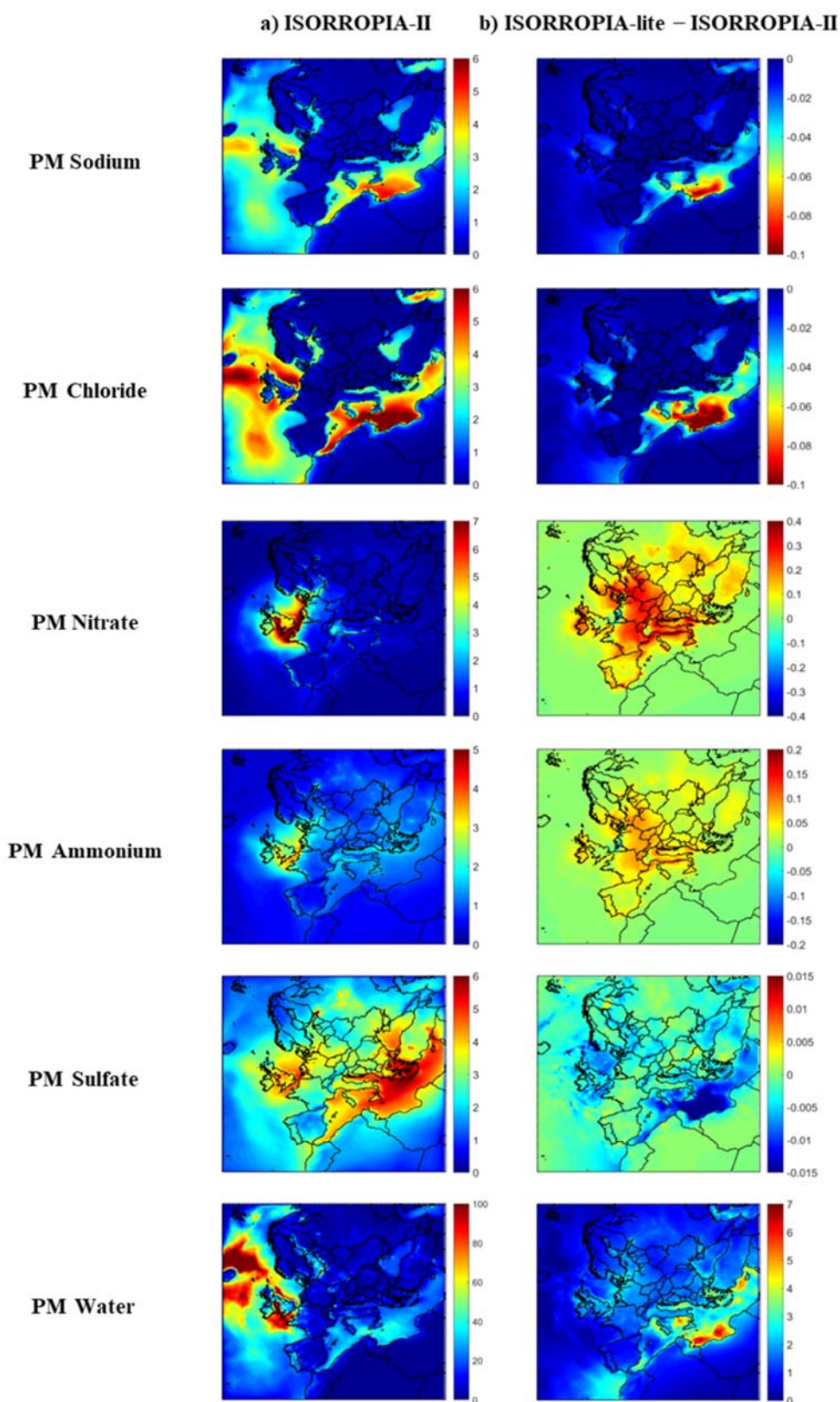


Figure 3.2. Average ground-level PM_{10} concentrations (in $\mu g m^{-3}$) of **a)** sodium, **b)** chloride, **c)** nitrate, **d)** ammonium, **e)** sulfate, and **f)** water using the default ISORROPIA-II and ISORROPIA-lite without organic water during May 2008.

Sodium and chloride concentrations are higher over water and lower over the continental Europe as expected. When we used ISORROPIA-lite for the simulation of aerosol thermodynamics in PMCAMx, sodium

and chloride predicted concentrations decreased on average by approximately 0.6%. The maximum difference of $0.2 \mu\text{g m}^{-3}$ over the central Mediterranean Sea occurs because of the physical state of the aerosol in ISORROPIA-lite (metastable state), which increases the dry deposition rate of the hygroscopic sea salt.

Predicted nitrate concentrations exceed $7 \mu\text{g m}^{-3}$ over the Netherlands, Belgium, United Kingdom, and northern France, while for the rest of Europe smaller concentrations are predicted (up to $3 \mu\text{g m}^{-3}$) when ISORROPIA-II is used. Using ISORROPIA-lite caused an increase on average nitrate concentration of approximately 10%. More specifically, average nitrate increased up to $0.4 \mu\text{g m}^{-3}$ over most of continental Europe except Belgium and Netherlands, where an average decrease of $0.1 \mu\text{g m}^{-3}$ is predicted.

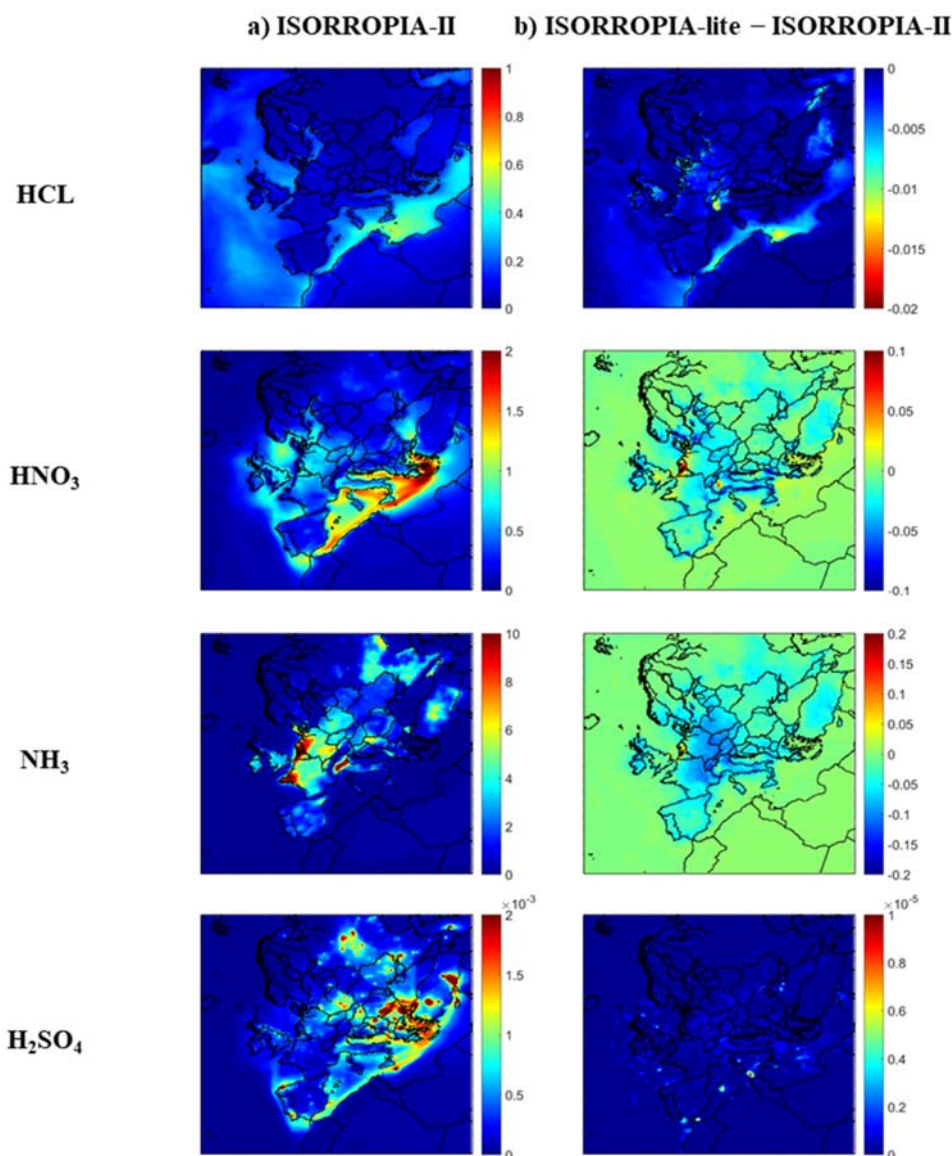


Figure 3.3. Average predicted ground-level concentrations (in ppb) of **a)** hydrochloric acid, **b)** nitric acid and **c)** ammonia using the default ISORROPIA-II and ISORROPIA-lite without organic water during May 2008.

Ammonium levels up to $3.5 \mu\text{g m}^{-3}$ are predicted in areas with high nitrate concentrations. It exists mainly as ammonium sulfate and ammonium nitrate when the default version of ISORROPIA-II is used. Ammonium increased on average by 2% when we used ISORROPIA-lite. More specifically, average ammonium concentrations increased up to $0.1 \mu\text{g m}^{-3}$ and decreased by $0.05 \mu\text{g m}^{-3}$ in the same areas where nitrate did.

Sulfate concentrations using ISORROPIA-II are high over the Mediterranean and neighboring countries such as Italy and Greece (up to $6 \mu\text{g m}^{-3}$), while for the rest of Europe concentrations less than $5 \mu\text{g m}^{-3}$ are predicted. Using ISORROPIA-lite caused a negligible decrease over the Mediterranean Sea of $0.02 \mu\text{g m}^{-3}$ and a negligible increase of $0.01 \mu\text{g m}^{-3}$ over continental Europe on sulfate.

Water concentrations are enhanced over the marine areas because of the existence of hygroscopic sea salt and are lower over continental Europe. As expected, due to the assumed metastable state of ISORROPIA-lite for low RH values, water concentration increased on average by 6.5%. More specifically, an increase of $1\text{--}2.5 \mu\text{g m}^{-3}$ is predicted over continental Europe while over the Mediterranean Sea higher increases are predicted (up to $7 \mu\text{g m}^{-3}$).

Hydrochloric acid is predicted to have higher concentrations over water especially in the Mediterranean Sea (up to 0.5 ppb), while in the rest of Europe less than 0.25 ppb are predicted when ISORROPIA-II is used (Fig 3.3). When ISORROPIA-lite is used, average hydrochloric acid concentration decreased by 0.8%, especially over the Mediterranean Sea and northern Italy.

Nitric acid concentrations are higher over the Mediterranean Sea (up to 2 ppb) than the rest of Europe, where concentrations less than 1 ppb are predicted (Fig. 3.3). Using ISORROPIA-lite caused an average decrease of 2%. Average nitric acid concentrations increased by 0.07 ppb over Belgium, northern Italy and Netherlands, while in the rest of Europe decreases up to 0.07 ppb are predicted. These results are consistent with the predicted PM nitrate behavior since when there is a decrease of the gas phase concentration, an increase of the particulate phase is predicted and vice versa.

Average ammonia concentrations are higher over Belgium, Netherlands, northern France and northern Italy mainly because of high agricultural emissions (Fig. 3.3). When ISORROPIA-lite is used ammonia decreased on average by 2%. As expected, ammonia increased by 0.07 ppb over Belgium and Netherlands, while in the rest of Europe decreases up to 0.07 ppb are predicted as nitric acid did.

The computational time needed for the entire simulation during May 2008 by PMCAMx using the default version of ISORROPIA-II was 64 CPU hr. Using ISORROPIA-lite for the simulation of aerosol thermodynamics in PMCAMx reduced the required computational time by approximately 6 CPU hr (9% reduction).

3.4 Summary of ISORROPIA-lite testing results

In terms of computational speed, for the partitioning problem simulation ISORROPIA-lite accelerates the calculations by 35% in the off-line tests and 9% in PMCAMx. In terms of composition, for the partitioning (forward) problem the discrepancies between the ISORROPIA-lite and ISORROPIA-II predictions for the concentrations of the various semivolatile aerosol components were generally low (less than 25%) in the off-line tests. Most of these discrepancies in the predictions of the two modules were found at low to intermediate RH range. However, these discrepancies should not be viewed as errors of ISORROPIA-lite, since in some cases the metastable state may be closer to the truth. These results indicate that ISORROPIA-lite considerably accelerates the thermodynamic calculations with the small cost of introducing some discrepancies in the inorganic aerosol predictions making it more suitable than ISORROPIA-II for ESMs.

3.5 Simulation of distribution of condensing nitrates on fine and coarse modes

The assumption of thermodynamic equilibrium is a good approximation for fine-mode aerosols that can reach equilibrium very fast. However, the equilibrium timescale for large particles is typically larger than the time step of the model (Meng and Seinfeld, 1996). To account for kinetic limitations, the process of gas/aerosol partitioning is proposed to be calculated in two stages (Pringle et al., 2010).

- In the first stage the amount of the gas-phase species that is able to kinetically condense onto the aerosol phase within the model time step is calculated, assuming diffusion limited condensation (Vignati et al., 2004). The calculation uses an accommodation coefficient for each species, this was taken as 0.1, 0.064 and 0.09 for HNO_3 , HCl , NH_3 respectively.
- In the second stage, ISORROPIA-light redistributes the mass between the gas and the aerosol phase, assuming instant equilibrium between the two phases.

It is implicit in this treatment that gas/aerosol partitioning starts from small to large particles (using the residual gases), since smaller particles equilibrate faster, because of the larger surface to volume ratio.

3.6 Nitrates and dust

Minerals present in dust, such as calcite, influence aerosols' pH and thus the distribution of nitrate between the gas and particulate phases.. Commonly, Earth System Models assume a globally uniform dust composition. Within FORCeS a new climatology of dust composition has been developed and it will be used by the corresponding ESMs, allowing them to characterize regional changes in dust composition and its potential impact on aerosols' pH and nitrate. The 3D mineral composition climatology relies on simulations done with the Multiscale Online Nonhydrostatic Atmosphere Chemistry (MONARCH) model (Pérez et al., 2011; Haustein et al., 2012; Jorba et al., 2012; Klose et al., 2021), which explicitly represents the atmospheric cycle of different minerals present in dust (Gonçalves-Ageitos et al., in prep).

The brittle fragmentation theory (Kok et al. 2011) has been applied to represent the size-resolved fractional dust mineralogy at emission in MONARCH, following Perlwitz et al. (2015a, 2015b). MONARCH describes the size distribution through a sectional approach, considering 8 bins per mineral from 0.2 to 20 μm in diameter. The underlying soil composition information has been taken from two different sources, Claquin et al. (1999), with the modifications included by Nickovic et al. (2012), and Journet et al. (2014), which will ultimately provide a measure of mineral composition uncertainties and allow assessment of the sensitivity of ESMs to changes in mineral fractions. The Claquin et al. (1999) Soil Composition Atlas considers 8 different minerals, namely: illite, smectite/montmorillonite, kaolinite, calcite, gypsum, hematite, quartz, and feldspars, while Journet et al. (2014) characterizes also vermiculite, chlorite, goethite, mica.

MONARCH has been run at the global scale, with $1^\circ \times 1.4^\circ$ of horizontal resolution and 48 vertical layers up to 10 hPa, for a period of 5 years (with one year of spin-up) using the Claquin et al. (1999) Global Soil Atlas as a basis. This dust composition climatology can be used by FORCeS models in the original model grid and with the MONARCH size distribution or as proportions in bulk dust. As an example, the proportion of calcite (%w at the surface) as derived from this climatology is depicted in Figure 3.4.

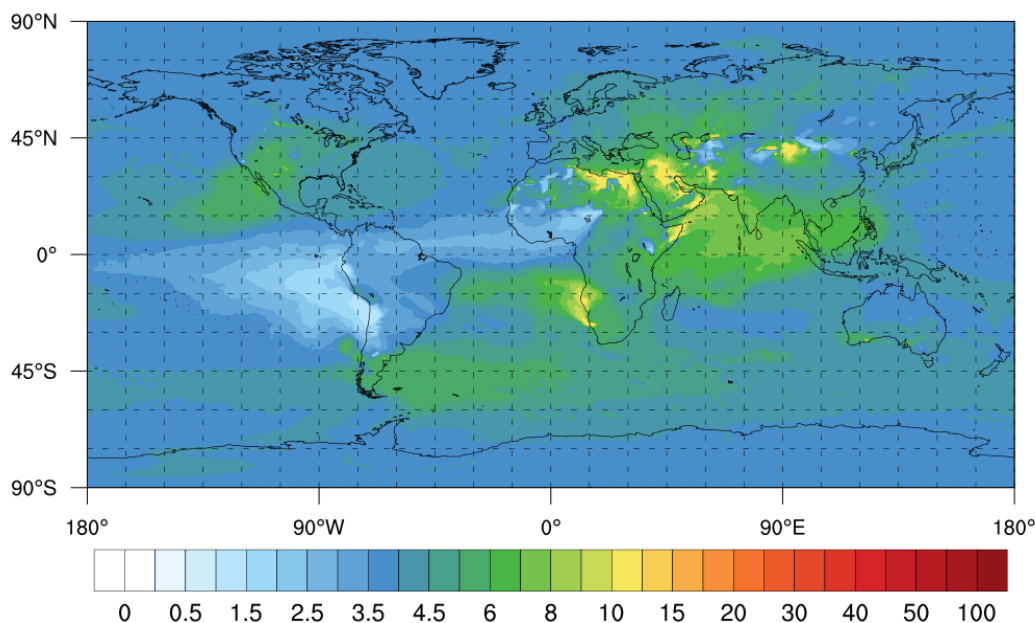


Figure 3.4. Annual mean calcite mass fraction (%w) at the surface as derived from MONARCH, 2007-2011, using the Claquin et al. (1999) Soil Atlas as a basis.

This 3D monthly-varying climatology can be interpolated to selected pressure levels (as opposed to original MONARCH vertical levels) and can be adapted to the ESMs size distribution (e.g. accumulation and coarse

modes in NorESM or EC-Earth). An alternative climatology making use of the Journet et al. (2014) Soil Atlas is also available.

In addition to the aforementioned mineral climatologies, a size-resolved mineral fraction at emission for the EC-Earth ESM has also been generated, by applying the brittle fragmentation theory and using both Claquin et al. (1999) and Journet et al. (2014) Soil Atlases as a basis (e.g. calcite fraction in the accumulation and coarse modes of EC-Earth is depicted in Figure 3.5).

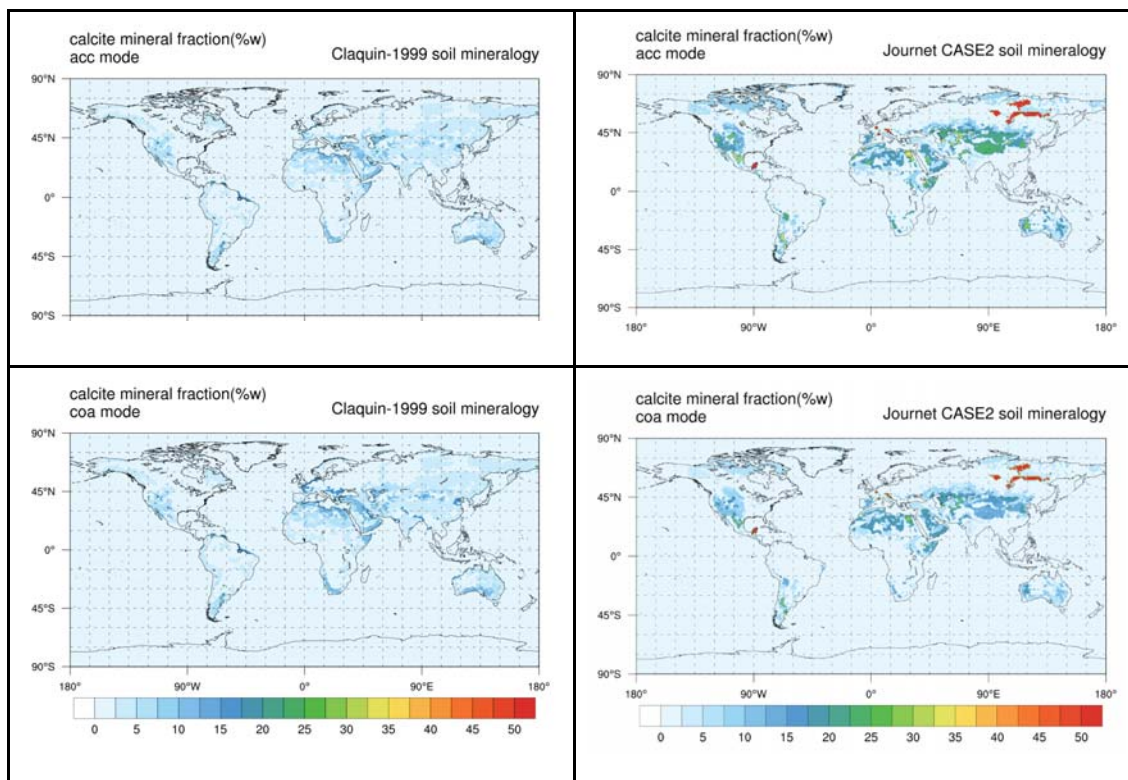


Figure 3.5. Calcite fraction at emission using Claquin-1999 (left) and Journet-2014 (right) for the accumulation (up) and coarse (down) modes in EC-Earth. These fractions are applied to the dust emission flux in each model.

Therefore the fine and coarse nitrate formation in EC-Earth accounts for calcium calculated online.

4. Organic and Other Aerosol Absorption

Absorbing organic aerosols are treated with simple approximations in ESMs. Currently, FORCES ESMs assume an organic aerosol with a weak absorption level (refractive imaginary index between 0.005 and 0.006). While this assumption represents a first approximation for the inclusion of a proper treatment of absorbing organic aerosols, namely brown carbon (BrC), it fails to reproduce strong gradients observed close to sources (e.g., biomass burning). Table 4.1 summarizes different parameterizations of BrC proposed in the literature. Based on this, several sensitivity runs have been performed with the MONARCH model to assess the impact of BrC representation with increasing complexity. Three main approaches are considered:

- Case 1: simple treatment of an organic aerosol with weakly absorbing properties similar to FORCES ESMs.
- Case 2: intermediate complexity with the Inclusion of a strongly absorbing BrC tracer from biomass burning emissions and variability of the imaginary refractive index from the hydrophobic to the hydrophilic modes.
- Case 3: complex treatment of BrC considering the primary emission (biomass and biofuel burning emissions), secondary aerosol formation with absorbing properties from anthropogenic precursors, and photobleaching chemical aging.

Table 4.1. Summary of BrC treatment in global models.

Reference	Number of BrC tracers	BrC emissions	Aging processes	Refractive index
Park et al. (2010)	None	No BrC emissions	BrC concentrations scaled from BrC/BC mass ratio of 0.5	BrC $n = 1.67 + 0.27i$
Feng et al. (2013)	Primary BrC	66% of BB/BF primary organic aerosol emissions	-	BrC $n = 1.65$ Moderately abs BrC $k = 0.075$ (350 nm), 0.02 (450 nm), 0.003 (550 nm), 0.0003 (650 nm) Strongly abs BrC $k = 0.168$ (350 nm), 0.063 (450 nm), 0.03 (550 nm), 0.005 (650 nm)
Lin et al. (2014)	Primary BrC and BrC-SOA	100% of BB/BF primary organic aerosol emissions	100% of SOA is BrC	BrC $n = 1.53$ High-absorbing BrC $k = 0.168$ (350 nm), 0.112 (400 nm), 0.063 (450 nm), 0.045 (500 nm), 0.030 (550 nm), 0.017 (600 nm), 0.005 (650 nm), 0.001 (700 nm) Low-absorbing BrC $k = 0.0738$ (350 nm), 0.025 (400 nm), 0.0066 (450 nm), 0.0024 (500 nm), 0.0010 (550 nm), 0.0004 (600 nm), 0.0002 (650 nm), 0.0001 (700 nm)
Wang et al. (2014)	Primary BrC and BrC-SOA	25% of BB and 50% of BF primary organic emissions	Aromatic SOA is BrC	BrC-POA MAE (440 nm) = $1 \text{ m}^2 \text{ g}^{-1}$ BrC-SOA MAE (440) = $0.3 \text{ m}^2 \text{ g}^{-1}$
Saleh et al. (2015)	No explicit BrC Tagging BB/BF POA-SOA	-	Absorption from BB/BF POA and SOA	OA $n = 1.78$ OA k as a function of BC-to-OA ratio of BB/BF emissions (Saleh et al., 2014)
Jo et al. (2016)	Primary BrC and BrC-SOA	Primary BrC BB/BF emissions parametrized using Modified Combustion Efficiency	Aromatic SOA with high atmospheric aging is BrC (first two bins VBS)	BrC-POA MAE = $5.3 \text{ m}^2 \text{ g}^{-1}$ (365 nm), $1 \text{ m}^2 \text{ g}^{-1}$ (550 nm) BrC-SOA MAE = $1.5 \text{ m}^2 \text{ g}^{-1}$ (365 nm)
Wang et al. (2018)	No explicit BrC Tagging BB/BF POA and aromatic SOA	-	Absorption from BB/BF POA and aromatic SOA Photobleaching of BB/BF POA parameterization based on OH and BrC half-life time of 1 day with a threshold of 25% of the original absorption value	POA k as a function of BC-to-OA ratio of BB/BF emissions (Saleh et al., 2014) BrC-SOA MAE = $1.46 \text{ m}^2 \text{ g}^{-1}$ (365 nm)
Brown et al. (2018)	No explicit BrC Tagging BB/BF POA	-	Photobleaching of BB/BF POA parameterization based on Wang et al. (2018) Absorption from SOA neglected	POA k as a function of BC-to-OA ratio of BB/BF emissions (Saleh et al., 2014)
Zhang et al. (2020)	Primary BrC and BrC-SOA	Primary BB/BF BrC emissions following Saleh et al. (2014).	Absorption from aromatic SOA Photobleaching of BB/BF Primary BrC parameterization with half-life of 12 h during daytime with a threshold of 6% of the original absorption value. Half-life of 12h in daytime for aromatic BrC-SOA until completely removed. POA effect: 12 h for primary BrC from BB and BF. SOA BrC: - Aromatic SOA 12-24 h, - limonene < 0.5 h, - Methylglyoxal SOA 90 min	BrC-POA MAE = $1 \text{ m}^2 \text{ g}^{-1}$ (550 nm) BrC-SOA MAE = $0.19 \text{ m}^2 \text{ g}^{-1}$ (550 nm) Primary BrC $k = 0.045$ (550 nm) BrC-SOA $k = 0.043$ (365 nm)

The MONARCH model was configured at the global scale following the three cases of absorption described above. The results of its simulations were evaluated against AERONET v3.0 inversion products aerosol optical depth (AOD), single-scattering albedo (w) and asymmetry parameter (g). The period of study is 2012-2016 where the AERONET Level 2 dataset is processed to derive as much daily data per month above a fixed threshold as possible (minimum of 20 daily data per month). It is well known that the lack of Level 2 inversion data is mostly due to the screening applied to measurements with AOD (440nm) > 0.4 (Li et al., 2014). To avoid this, a manual screening of the Level 1.5 data following all the quality-assurance criteria of Holben et al. (1998) except filtering for AOD(440 nm) has been applied. With this procedure, an almost Level 2 dataset without missing the majority of stations is obtained and used for the evaluation. As an example, Figure 4.1 shows results of Case 1, where the organic aerosol refractive index assumed is $1.53 + 0.006i$, at the AERONET site GSFC.

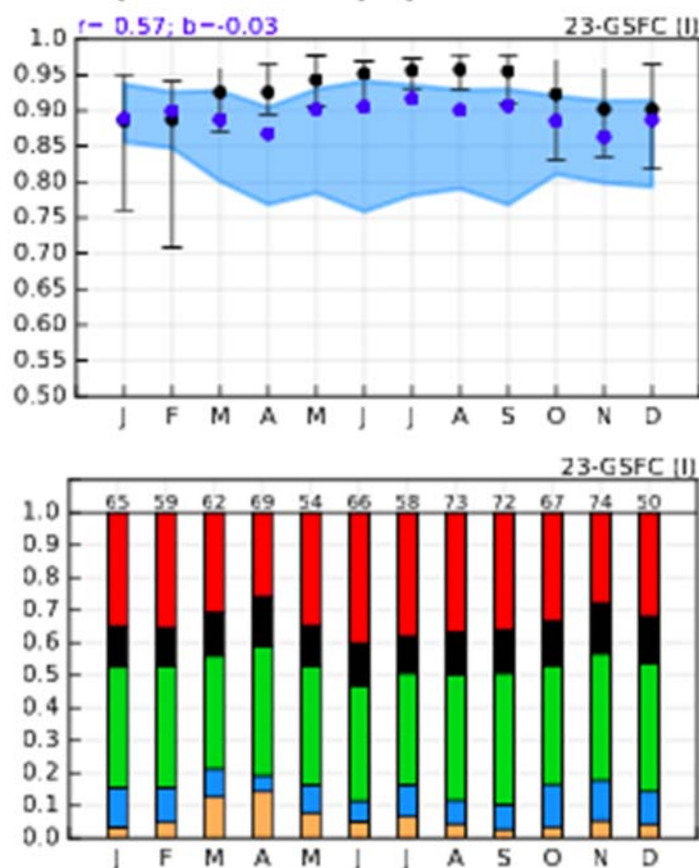


Figure 4.1 Monthly mean single-scattering albedo of the aerosol mixture in the MONARCH model (blue) and measured at GSFC AERONET site (black) for the period 2012-2016, and simulated monthly AOD fractions of sulfate (red), black carbon (black), organic aerosols (green), sea salt (blue) and mineral dust (orange).

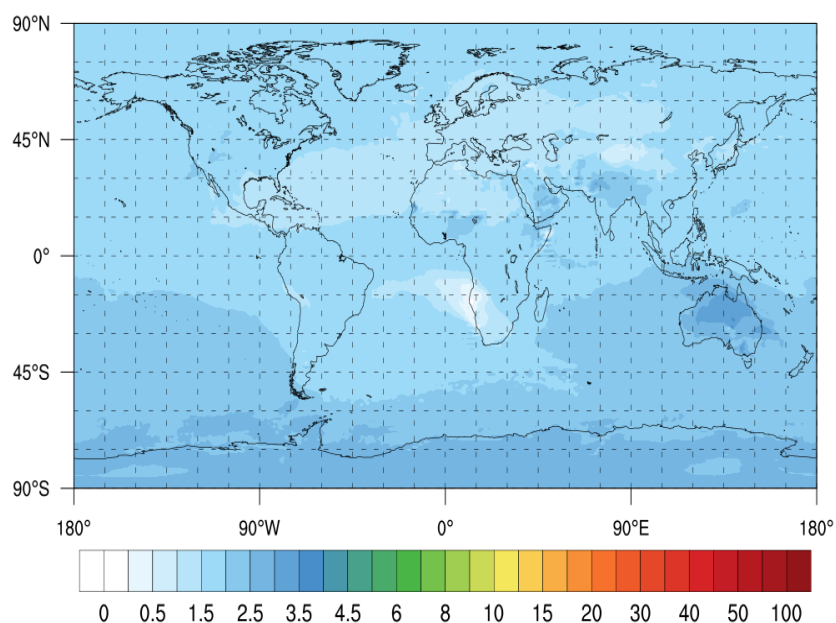


Figure 4.2 Annual mean iron oxides mass fraction (%w) at the surface as derived from MONARCH, 2007-2011, using Claquin et al. (1999) Soil Atlas as a basis.

These results will allow the better characterization of regional variations in dust optical properties within ESMs.

4.1 Absorption parameterization in ESMs

Black carbon is the main type of aerosol absorbing solar radiation and warming climate that is currently considered in most climate and Earth System Models. Dust aerosol is also weakly absorbing and parameterized in terms of an imaginary part in its refractive index. Accuracy in ESM simulations of absorption by dust rely on the accuracy of dust mineralogy in the models. The climatologies described in Section 3 will be used to improve this aspect of simulation of aerosol absorption.

Organic aerosols may also be rich in light-absorbing material. This so-called brown carbon (BrC) has received attention owing to its warming potential and impacts, especially in the upper atmosphere (Zhang et al., 2017, 2020). To account for this extra aerosol absorption most models are simply adding a small imaginary part to the refractive index of the organic aerosol (Tsigaridis and Kanakidou, 2018). This assumption however implies that BrC is a constant fraction of organic aerosol worldwide, while it is known that incomplete biomass burning and biofuel combustion, as well as secondary organic aerosol from the oxidation of aromatics produces BrC with different proportions to organic aerosol (Laskin et al. 2015; Zhang et al., 2020 and references therein). The secondary BrC is linked to the lowest volatility fraction extremely low volatility organics (Jo et al. 2013; Saleh et al., 2014; Tasoglou et al., 2020). Explicit consideration of BrC absorption in ESMs requires first setting the imaginary part of the refractive index of organic aerosols to zero.

Zhang et al. (2020) have shown that BrC absorption is geographically non-uniform and can be a large fraction of the aerosol absorption in particular in the tropical free troposphere, exceeding regionally that of black carbon (Figure 4.3). They have also shown the different geographic patterns of the three studied sources of BrC (biomass burning, biofuel and secondary formation from aromatic oxidation). Explicit consideration of BrC absorption will improve the geographic distribution of aerosol absorption effect on climate. Introducing BrC absorption in the ESMs requires assuming only scattering properties for organic aerosol in the model. Because BrC is a minor component of organic aerosol in terms of mass, it is recommended to parameterize in the ESMs only the absorption by BrC and not its mass concentration. This approach, that leaves unaffected the organic aerosol parameterizations in the ESMs, is supported by the fact that BrC is measured as absorption (not as mass) and therefore comparison of model results has to be done against optical properties.

Studies to date show that BrC in ambient aerosol can be classified in roughly two types (Figure 4.4), one that is reactive and loses its absorbing properties by photobleaching (photolysis and reaction with OH) with an e-folding time of about 11 h during daytime ($k=3.4 \times 10^{-5} \text{ s}^{-1}$, Wong et al., 2019; Skyllakou et al. in preparation) and the other one that is inert and is removed from the atmosphere only by deposition.

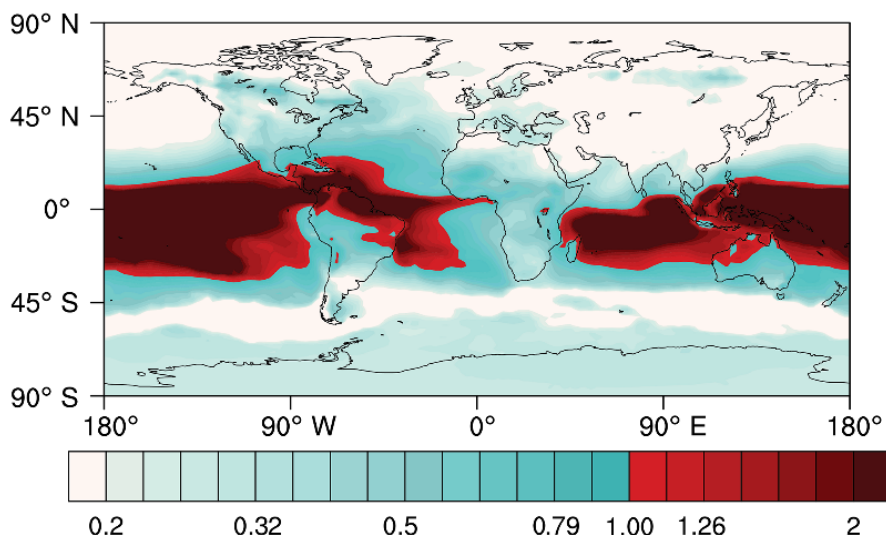


Figure 4.3: Annual mean ratio of Direct Radiative Effect (DRE) of BrC to that of black carbon (figure from Zhang et al., 2020).

The inert BrC tends to be of large molecular weight typically associated with humic-like substances, while the reactive BrC tends to have a much lower molecular weight (Wong et al., 2019). In particular, Wong et al. (2019) studied the reactivity of BrC from the atmospheric samples collected from the East Mediterranean during biomass burning events and concluded that biomass burning BrC across all molecular weights has an atmospheric lifetime of 15 to 28 h. Zhang et al. (2020) based on the observations by Forrister et al. (2015) on ambient BrC from wildfires in the Western United States assumed a 6% of primary BrC emissions to be persistent. Wang et al. (2018) and Brown et al. (2018) in their models applied a 1 d e-folding time for BrC before reaching a threshold of 25% of the original BrC absorption.

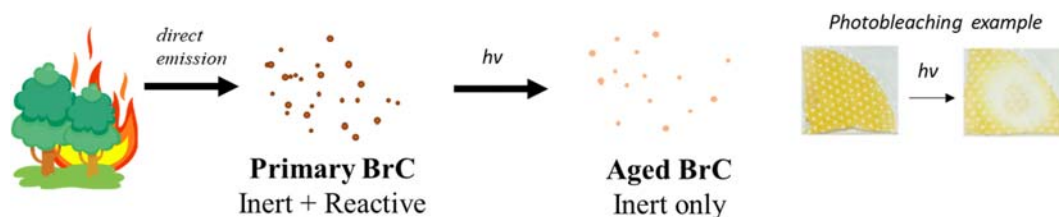


Figure 4.4. Concept of the atmospheric behavior of emitted BrC. Figure adopted from Skyllakoy et al., in preparation. Here, biomass burning is a source of BrC which contains an inert fraction that resists photo-oxidation and a reactive fraction that decays over ~ 1 day atmospheric residence.

Skyllakou et al. (in preparation), also consider BrC in the PMCAMx model, and assume that it originates from biomass burning, being composed of “inert” BrC (10% of the total emitted) and “reactive” BrC (the remaining 90%). This BrC is explicitly treated as distinct chemical species – with concentration that reproduces the absorption (Mass absorption coefficient) of fresh biomass burning aerosol (Wong et al., 2019; Forrister et al., 2015). Both types of BrC are assumed non-volatile (i.e., they are placed in the least volatile bin of the PMCAMx model, $C^*=0.01 \mu\text{g m}^{-3}$). Reactive BrC decays with a first order reaction with a kinetic constant of $k=3.4 \times 10^{-5} \text{ s}^{-1}$ ($\sim 11\text{hr}$ daytime lifetime), consistent with Wong et al. (2019) for BrC from wildfires in the E.Mediterranean. Results of their work is shown in Figure 4.5. The distributions of black carbon, primary and total biomass burning organic aerosol have been evaluated elsewhere. The corresponding distributions of inert BrC and reactive BrC show distributions that are consistent with their source regions; the reactive BrC

mostly decays within one day of transport – consistent with the kinetics prescribed. The impact of the BrC on the aerosol optical properties and radiative forcing is ongoing research.

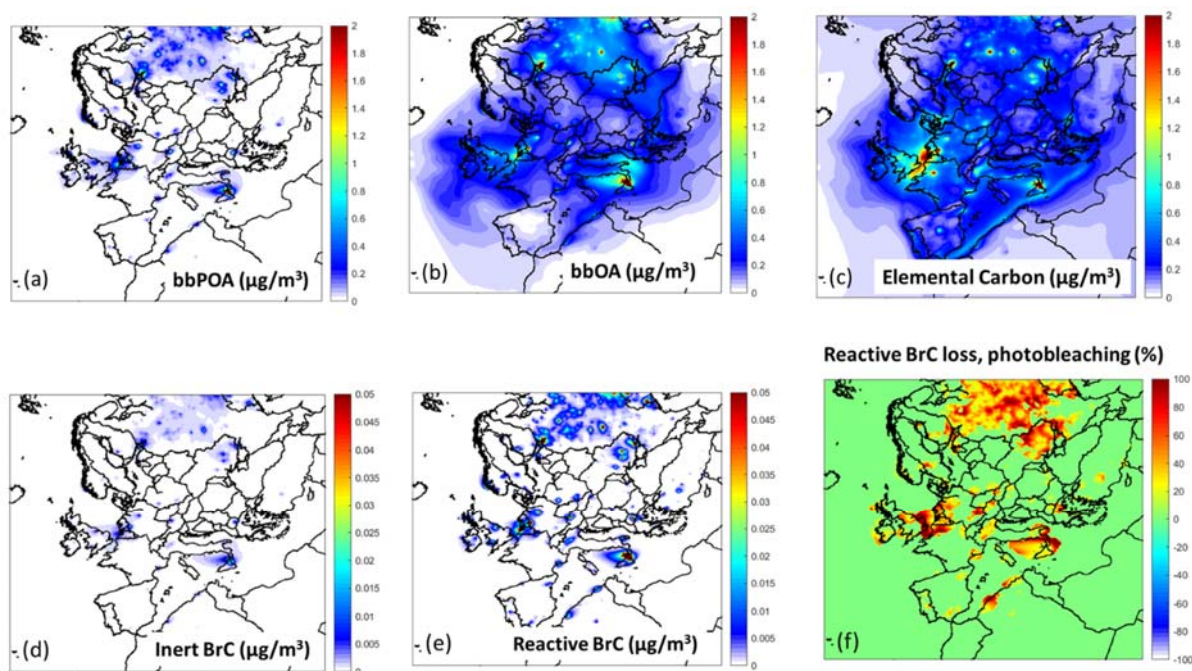


Figure 4.5. Simulations of biomass burning (BB) aerosol components with the PMCAMx model (Skyllakoy et al., in preparation). Results corresponding to 29-day average for May, 2008. Distributions of (a) BB primary organic aerosol, (b) BB total organic aerosol, (c) elemental carbon, (d) inert BrC from BB, and (e) reactive BrC from BB.

4.2 Proposed BrC implementation in ESMs

There are two approaches proposed to account for BrC absorption in ESMs. First to be performed is the explicit consideration of BrC absorption. This will also enable calculation of the 3-d monthly mass absorption coefficients (MAC) that can be applied on OA (3-d) fields per month and provide equivalence to BrC absorption. The simplified approach will use these 3-d monthly varying MAC fields instead of an explicit consideration of BrC absorption. In both cases, the organic aerosol has to be changed to scattering only and any absorption related to organics is considered in the BrC absorption.

The look up tables of aerosol optical properties need to be extended to account for BrC (extinction, asymmetry factor).

Three different BrC species are to be considered (two primary species and one secondary from aromatics oxidation). The one primary BrC is inert, not losing its absorbing properties, while the other two BrC species rapidly lose their absorbing properties. All species are in the accumulation mode and subject to atmospheric deposition. For primary BrC the imaginary part of refractive index of 0.045 at 550 nm and for secondary BrC that of 0.043 at 365 nm have been estimated by Liu et al. (2013) and Zhang et al. (2020) and depend on wavelength (Saleh et al., 2014).

Primary BrC sources to be considered are from biomass burning and biofuel combustion that can be calculated (as mass equivalent to absorption) as explained in Zhang et al. (2020) using the BC/OA emission ratio and keep them external to the microphysics model of the ESM, or associate them to the ELVOC species in the model (correlation experimentally shown by Tasoglou et al. (2020) and adopted by Skylakou et al. (in preparation)).

Evaluation of model results will be done for absorbing aerosol as a whole against AERONET data and for BrC using available measurements. Aeronet data of AOD, SSA and AAOD and asymmetry factors filtered with size and optical properties parameters to distinguish absorbing aerosols (BrC, BC) and dust/iron oxides as in Schuster et al. (2016) will be used. A fraction of ATOM datasets, which includes BrC measurements from

aircraft campaigns during 2016-2018 (Zeng et al. 2020), as well as DC3 and SEAC4RS campaigns during 2012-2013 (Toon et al., 2016) will be also used for model evaluation.

5. Ultrafine Particles

There are several efforts in FORCeS to improve the parameterizations that are currently used in ESMs for the simulation of the ultrafine particles and the corresponding aerosol number distribution. The work has been focused on the improvement of the simulation of the new particle formation/growth processes and on the treatment of number emissions. Our objective is once more to improve accuracy with a small computational cost for the ESMS.

5.1 Parameterization of new particle formation and growth rates

The new parameterizations of formation rates developed in FORCeS are based on analyses of atmospheric particle number-size distribution (PNSD) measurements (Kulmala et al., 2012). All measurements have been performed at the University of Helsinki SMEAR II station in Hyytiälä, Finland. Clear new-particle formation (NPF) events are identified from the PNSD data. During times of these NPF events, the formation rates are calculated from the PNSD according to:

$$J = \frac{dN}{dt} + CoagS \times N + \frac{GR}{\Delta dp} \times N$$

where N is the number concentration of particles in the considered size range, $CoagS$ is the coagulation sink due to larger pre-existing particles and the growth rate GR determines the condensational growth out of the considered particle size range. Several particle size ranges (3-6, 6-10, 10-14 nm) were analyzed for the formation rates. Here we present results of formation rates for 6–10 nm and 10–14 nm particles, which are called J_6 and J_{10} , respectively. These size ranges were chosen in order to capture the effects of both the nucleation and the subsequent early growth of particles. Distinguishing particles originating from NPF from the background particles becomes challenging in atmospheric PNSD measurements when analyzing concentrations of particles larger than 10–20 nm.

Sulphuric acid has been identified as an important precursor vapor for NPF in atmospheric conditions at various environments (e.g. Kerminen et al., 2018). Additionally, oxidation products of volatile organic compounds have been observed to participate in the first steps of new particle formation and growth of the particles (Ehn et al., 2014; Jokinen et al., 2015). Here we utilize data from CI-API-TOF mass spectrometer measurements of concentrations of sulphuric acid (H_2SO_4) and highly-oxidized organic molecules (HOM; molecular mass range of 260-622 amu).

Several functional forms were considered for the parameterizations involving different combinations of sulphuric acid and HOM concentrations. In earlier analyses of atmospheric NPF it has been found that particle formation rates are typically connected to linear or squared dependencies on concentrations of H_2SO_4 and low-volatility vapours or the products of these vapour concentrations (Paasonen et al., 2010). Therefore, we have used these types of parameterizations as the starting point for the analyses here. Figure 5.1 presents the correlation between the parameterized and measured formation rates of 10 nm particles, using the parameterization

$$J_{10} = [H_2SO_4]^2 + [H_2SO_4] \times [HOM] + [HOM]^2.$$

where $[H_2SO_4]$ and $[HOM]$ are the corresponding gas-phase concentrations. The formation rates are daily medians calculated between 9:00 – 12:00, which is the typical time window when nucleation mode particle formation and growth is occurring during NPF event days in Hyytiälä.

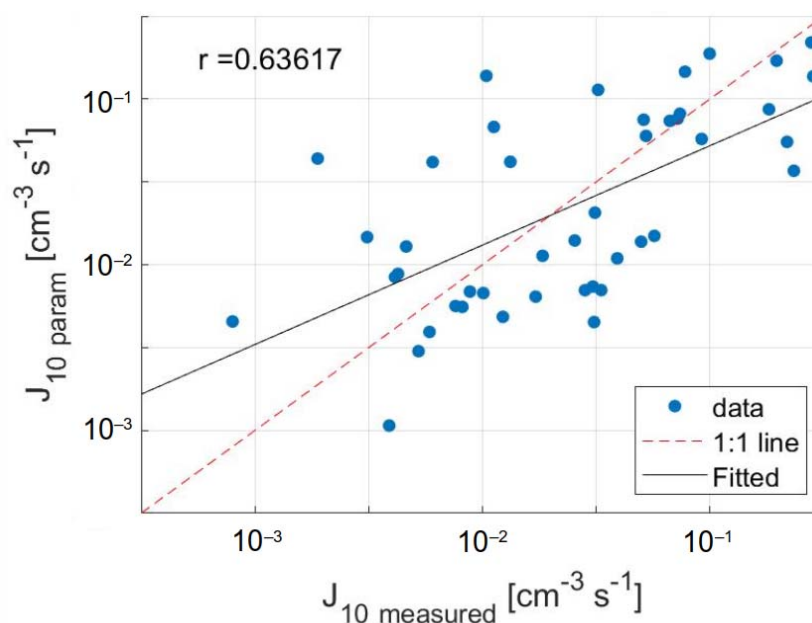


Figure 5.1. The correlation between the daily parameterized median formation rate of 10 nm particles ($J_{10,param}$) and the measured formation rate ($J_{10,measured}$) in Hyytiälä. The parameterization of daily values is based on the sum of squared vapor concentrations ($[H_2SO_4]^2$ and $[HOM]^2$) and product of the concentrations ($[H_2SO_4] \times [HOM]$). Correlation coefficient between the parameterized and measured formation rates is 0.63, the dashed line indicates the one-to-one correspondance and the solid line is the least-squares fit between the $J_{10,param}$ and $J_{10,measured}$.

The resulting fitting coefficients for three different types of formation rate parameterizations for both J_6 (6–10 nm particles) and J_{10} (10–14 nm particles) are given in Table 5.1. The correlation between the hourly measured and parameterized J values for all these versions of the parameterizations are approximately 0.5. The parameterizations for J_6 seem to perform slightly better than for J_{10} , but overall it cannot be concluded that either the parameterization for J_6 or J_{10} would be clearly better.

Table 5.1. Fitting coefficients for the formation rate parameterizations of the hourly measured J_6 and J_{10} in Hyytiälä, Finland. The fittings are made at timescale of one hour, and the correlation coefficients show the correlation between the measured and parameterized formation rates.

	J_6		J_{10}	
Parameterization	Fitting coefficients	R	Fitting coefficients	R
$a \times [H_2SO_4] + b \times [HOM]$	$a = 1.55 \times 10^{-8} \text{ s}^{-1}$ $b = 3.5 \times 10^{-11} \text{ s}^{-1}$	0.51	$a = 1.41 \times 10^{-8} \text{ s}^{-1}$ $b = 1.19 \times 10^{-10} \text{ s}^{-1}$	0.47
$a \times [H_2SO_4]^2 +$ $b \times [H_2SO_4] \times [HOM]$	$a = 1.08 \times 10^{-19} \text{ cm}^3 \text{ s}^{-1}$ $b = 4.55 \times 10^{-16} \text{ cm}^3 \text{ s}^{-1}$	0.51	$a = 1.8 \times 10^{-19} \text{ cm}^3 \text{ s}^{-1}$ $b = 6.2 \times 10^{-16} \text{ cm}^3 \text{ s}^{-1}$	0.49
$a \times [H_2SO_4]^2 +$ $b \times [H_2SO_4] \times [HOM] +$ $c \times [HOM]^2$	$a = 1.14 \times 10^{-13} \text{ cm}^3 \text{ s}^{-1}$ $b = 1.34 \times 10^{-15} \text{ cm}^3 \text{ s}^{-1}$ $c = 1.23 \times 10^{-19} \text{ cm}^3 \text{ s}^{-1}$	0.52	$a = 1.61 \times 10^{-14} \text{ cm}^3 \text{ s}^{-1}$ $b = 3.71 \times 10^{-16} \text{ cm}^3 \text{ s}^{-1}$ $c = 1.29 \times 10^{-19} \text{ cm}^3 \text{ s}^{-1}$	0.48

5.2 Parameterization of sub-grid processing of number emissions

A method for parameterizing sub-grid scale aerosol dynamics of freshly emitted aerosol is extended for application to ESMs. This approach is based on the calculation of the probability that a given particle emitted inside a computational grid cell will survive and be available for transfer outside the cell. This approach is based on the work of Pierce et al. (2009) and has not been used in any ESMs. This survival probability is

calculated as a function of the emitted particle size, the pre-existing aerosol size distribution and the grid-cell mean advection time scale. The approach can be used in ESMs at all scales.

One of the major challenges in simulating the aerosol number concentration and number distribution in regional or global atmospheric scales is the description of aerosol dynamics near sources of primary particles. These emission “hot spots” are usually large urban areas in global models. Most models “spread” the effect of the hot spot unrealistically across the computational cell. Because coagulation does not conserve particle number, the artificial spreading of the emitted particles does not account for the reduction of the number of particles through coagulation as they disperse through the grid cell. This means that particles that should not survive long enough to leave the source grid cell may be artificially advected to adjacent cells. This causes a potentially significant high bias of particle number in the transport of particles between grid cells. Additionally, the spreading of particle number concentrations from “hot spots” into “background” portions of a model grid cell complicates comparison of model predictions with point observations and may bias predictions of aerosol indirect radiative forcing. Simulation of the rapid dilution of particles as they disperse away from their source together with their coagulation and removal is prohibitively expensive for ESMs.

Our hypothesis is that once the aerosol source plume has dispersed in background air for several minutes, coagulation of freshly emitted particles with pre-existing particles is the dominant removal process of the freshly emitted aerosols in the lengthscales/timescales of ESMs. This simplification allows the loss of freshly emitted particles to be parameterized using the size-dependent timescale of coagulation with pre-existing particles and the timescale for advection through the grid cell.

5.2.1 The sub-grid coagulation parameterization

Throughout this section we will derive equations involving the aerosol size distribution in its general continuous form. The translation to sectional, modal or moment representations is straightforward. The sub-grid coagulation parameterization as proposed by Pierce et al. (2009) determines the fraction of freshly emitted particles that will survive without coagulating with pre-existing particles during a given time, τ . This survival probability depends on the size-dependent coagulation-loss timescale (Pierce and Adams, 2007):

$$\tau_{coag}(d_p) = \frac{1}{\int_{d_p}^{\infty} K(d_p, D_p) \cdot n_e(D_p) \cdot dD_p} \quad (5.1)$$

where d_p is the diameter of the freshly emitted particle, D_p is the diameter of a pre-existing particle, $\tau_{coag}(d_p)$ is the size-dependent coagulation-loss timescale, $K(d_p, D_p)$ is the coagulation kernel (Seinfeld and Pandis, 2006) and n_e is the number size distribution (dN/dD_p) of pre-existing particles. We assume implicitly that the larger of the two colliding particles is the particle that survives.

The survival probability or fraction of freshly emitted particles “surviving” after time τ , $P_s(d_p)$, is:

$$P_s(d_p) = \exp\left(\frac{-\tau}{\tau_{coag}(d_p)}\right) \quad (5.2)$$

The effective size-resolved number source rate accounting for sub-grid coagulation, E_{eff} , is then:

$$E_{eff}(d_p) = E_{src}(d_p) \cdot P_s(d_p) \quad (5.3)$$

where E_{src} is the size-resolved number emissions rate measured near the source at ambient conditions (after the emissions have cooled down and the initial nucleation/condensation and self coagulation has taken place) (Kittelson, *et al.*, 2002).

For mass conservation, the mass of the freshly emitted particles that coagulated with pre-existing particles must be added to the pre-existing particles. The fraction, F , of freshly emitted particles of size d_p that were lost by coagulation with pre-existing particles of size D_p , is equal to:

$$F(d_p, D_p) = \frac{K(d_p, D_p) \cdot n_e(D_p)}{\int_{d_p}^{\infty} K(d_p, D_p) \cdot n_e(D_p) \cdot dD_p} = K(d_p, D_p) \cdot n_e(D_p) \cdot \tau_{coag}(d_p) \quad (5.4)$$

The mass of the coagulated freshly emitted particles added to the pre-existing particles during τ depends on the size of the pre-existing particles:

$$M_{add}(D_p) = \frac{\pi\rho}{6} \int_0^{D_p} F(d_p, D_p) \cdot (E_{src}(d_p) - E_{eff}(d_p)) \cdot d_p^3 \cdot dd_p \quad (5.5)$$

In this equation, M_{add} is the mass to add to each pre-existing particle at time, τ , and ρ is the density of the freshly emitted particles.

The proposed survival probability ignores the effect of condensation/evaporation on freshly emitted particles. Condensation/evaporation grows or shrinks the freshly emitted particles to sizes where their coagulation rates are different. It is currently difficult to predict the condensation/evaporation rates of particles at the sub-grid level. The evaporation rates depend on the combustion source, background organic aerosol concentrations and the mixing rates. This evaporation will likely decrease the coagulation-loss timescale of the freshly emitted particles. Competing with this evaporation is the growth of particles due to the condensation of low-volatility compounds such as sulfuric acid or secondary organic aerosol that increase the coagulation-loss timescale of the freshly emitted particles. Due to the complexity of condensation/evaporation on the sub-grid level we are currently not including these effects on the coagulation-loss timescale. This could be the topic of future work.

A detailed comparison of the proposed parameterization against a model of aerosol dynamics has been presented by Pierce et al. (2009). A comparison of the results of the parameterization against the detailed model prediction is shown in Figure 5.2.

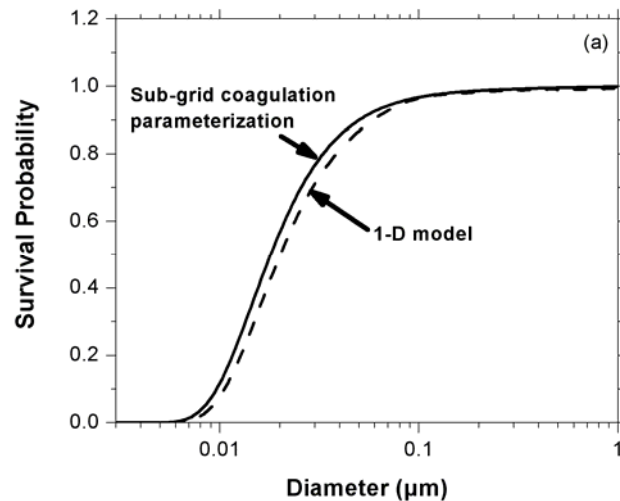


Figure 5.2. The size-dependent survival probability for a typical case based on the Pierce et al. (2009). The results of the parameterization are compared to these of a detailed 1-D Lagrangian model.

The error introduced by the parameterization depends on the ratio of the fresh particle mean size to that of the mean size of the pre-existing aerosol (Pierce et al., 2009). For most cases in which the fresh particles are on average smaller than the preexisting this error is less than 10% (Figure 5.3). However, even in the unusual cases in which there are a lot of very small particles present this error remains less than 20%.

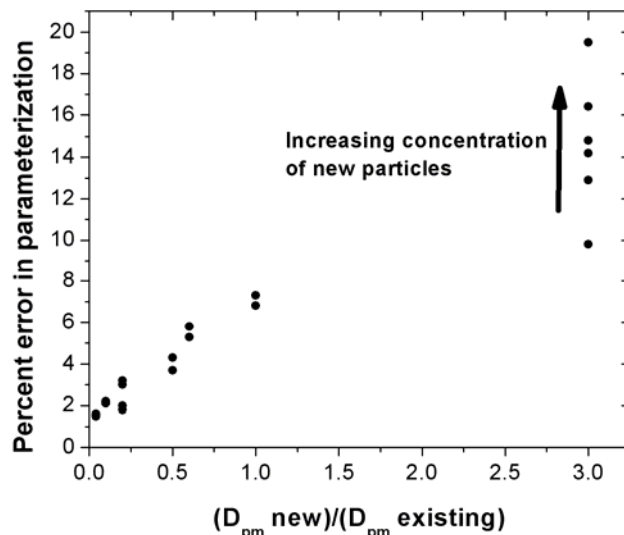


Figure 5.3. The percent error in the number of sub-micron particles left after three hours by using the sub-grid coagulation parameterization rather than the 1-D model as a function of the ratio of the median diameters of the freshly-emitted (new) and pre-existing (existing) particles based on Pierce

5.2.2 Application of the parameterization in ESMs

The goal of the sub-grid coagulation parameterization is to predict more accurately the transport of ultrafine particles between source grid cells and adjacent grid cells in ESMs. If the emissions are generated by a number of hot spots spread randomly about the middle of the grid cell, the time, τ , in Eqn. 5.2 should be chosen to reflect the grid-cell mean advection timescale (i.e. the mean time it takes for freshly emitted particles to be advected from the cell). This instantaneous grid-cell mean advection time scale, τ_{adv} , is:

$$\tau_{adv} = \frac{L}{2 \cdot U} \quad (5.6)$$

where L is the length or width of the grid cell and U is the wind speed of the grid cell. One issue with this instantaneously calculated value is that τ_{adv} goes to infinity when U is zero and all of the freshly emitted particles will be removed in the sub-grid coagulation parameterization. Because of this issue, it is necessary to put an upper bound on τ_{adv} . One may also choose to use a time-averaged advection time scale for several or all time steps rather than calculating the instantaneous timescale. After calculating the portion of the grid cell emissions that will survive advection to adjacent cells, these particles may be added to the source grid cell and the coagulated mass may be added to pre-existing particles using Eqns. 5.4 and 5.5.

6. References

Aiken, A. C., Decarlo, P. F., Kroll, J. H., Worsnop, D. R., Huffman, J. A., Docherty, K. S., Ulbrich, I. M., Mohr, C., Kimmel, J. R., Sueper, D., Sun, Y., Zhang, Q., Trimborn, A., Northway, M., Ziemann, P. J., Canagaratna, M. R., Onasch, T. B., Alfarra, M. R., Prevot, A. S. H., Dommen, J., Duplissy, J., Metzger, A., Baltensperger, U., and Jimenez, J. L.: O/C and OM/OC ratios of primary, secondary, and ambient organic aerosols with high-resolution time-of-flight aerosol mass spectrometry, *Environmen. Sci. & Technol.*, 42, 4478-4485, 2008.

Ansari, A. S. and Pandis, S. N.: Prediction of multicomponent inorganic atmospheric aerosol behavior, *Atmos. Environ.*, 33, 745-757, 1999a.

- Ansari, A. S. and Pandis, S. N.: An analysis of four models predicting the partitioning of semivolatile inorganic aerosol components, *Aerosol Sci. Technol.*, 31, 129–153, 1999b.
- Ansari, A. S. and Pandis, S. N.: The effect of metastable equilibrium states on the partitioning of nitrate between the gas and aerosol phases, *Atmos. Environ.*, 34, 157–168, 2000.
- Bentsen, M., Bethke, I., Debernard, J. B., Iversen, T., Kirkevåg, A., Seland, Ø., Drange, H., Roelandt, C., Seierstad, I. A., Hoose, C., and Kristjánsson, J. E.: The Norwegian Earth System Model, NorESM1-M – Part 1: Description and basic evaluation of the physical climate, *Geosci. Model Dev.*, 6, 687–720, 2013.
- Bougiatioti, A., Nikolaou, P., Stavroulas, I., Kouvarakis, G., Weber, R., Nenes, A., Kanakidou, M., and Mihalopoulos, N.: Particle water and pH in the eastern Mediterranean: source variability and implications for nutrient availability, *Atmos. Chem. Phys.*, 16, 4579–4591, 2016.
- Bromley, L. A.: Thermodynamic properties of strong electrolytes in aqueous solutions, *AIChE J.*, 19, 313–320, 1973.
- Brown, H., Liu, X., Feng, Y., Jiang, Y., Wu, M., Lu, Z., Wu, C., Murphy, S., and Pokhrel, R.: Radiative effect and climate impacts of brown carbon with the Community Atmosphere Model (CAM5), *Atmos. Chem. Phys.*, 18, 17745–17768, <https://doi.org/10.5194/acp-18-17745-2018>, 2018.
- Browne, E. C., Min, K. E., Wooldridge, P. J., Apel, E., Blake, D. R., Brune, W. H., Cantrell, C. A., Cubison, M. J., Diskin, G. S., Jimenez, J. L., Weinheimer, A. J., Wennberg, P. O., Wisthaler, A., and Cohen, R. C.: Observations of total RONO₂ over the boreal forest: NO_x sinks and HNO₃ sources, *Atmos. Chem. and Phys.*, 13, 4543–4562, 2013.
- Burgos, M., Andrews, E., Titos, G., Alados-Arboledas, L., Baltensperger, U., Day, D., Jefferson, A., Kalivitis, N., Mihalopoulos, N., Sherman, J., Sun, J., Weingartner, E., and Zieger, P.: A global view on the effect of water uptake on aerosol particle light scattering, *Scientific Data*, 6, <https://doi.org/10.1038/s41597-019-0158-7>, 2019.
- Burgos, M. A., Andrews, E., Titos, G., Benedetti, A., Bian, H., Buchard, V., Curci, G., Kipling, Z., Kirkevåg, A., Kokkola, H., Laakso, A., Letertre-Danczak, J., Lund, M. T., Matsui, H., Myhre, G., Randles, C., Schulz, M., van Noije, T., Zhang, K., Alados-Arboledas, L., Baltensperger, U., Jefferson, A., Sherman, J., Sun, J., Weingartner, E., and Zieger, P.: A global model–measurement evaluation of particle light scattering coefficients at elevated relative humidity, *Atmos. Chem. Phys.*, 20, 10231–10258, 2020.
- Capaldo, K. P., Pilinis, C., Pandis, S. N.: A computationally efficient hybrid approach for dynamic gas/aerosol transfer in air quality models, *Atmos. Environ.*, 34, 3617–3627, 2000.
- Carter, W. P. L.: Documentation of the SAPRC-99 Chemical Mechanism for VOC Reactivity Assessment, Report to California Air Resources Board, <http://intra.engr.ucr.edu/~carter> (last access: 8 January 2021), 2000.
- Claquin, T., Schulz, M., and Balkanski, Y. J.: Modeling the mineralogy of atmospheric dust sources, *Journal of Geophysical Research Atmospheres*, <https://doi.org/10.1029/1999JD900416>, 1999.
- Donahue, N. M., Robinson, A. L., Stanier, C. O., and Pandis, S. N.: Coupled partitioning, dilution, and chemical aging of semivolatile organics, *Environ. Sci. Technol.*, 40, 2635–2643, 2006.
- Donahue, N. M., Henry, K. M., Mentel, T. F., Kiendler-Scharr, A., Spindler, C., Bohn, B., Brauers, T., Dorn, H. P., Fuchs, H., Tillmann, R., Wahner, A., Saathoff, H., Naumann, K.-H., Moehler, O., Leisner, T., Mueller, L., Reinnig, M.-C., Hoffmann, T., Salo, K., Hallquist, M., Frosch, M., Bilde, M., Tritscher, T., Barmet, P., Praplan, A. P., DeCarlo, P. F., Dommen, J., Prevot, A. S. H., and Baltensperger, U.: Aging of biogenic secondary organic aerosol via gas-phase OH radical reactions, *Proceedings of the National Academy of Sciences of the United States of America*, 109, 13503–13508, [10.1073/pnas.1115186109](https://doi.org/10.1073/pnas.1115186109), 2012.
- Donahue, N. M., Chuang, W., Epstein, S. A., Kroll, J. H., Worsnop, D. R., Robinson, A. L., Adams, P. J., and Pandis, S. N.: Why do organic aerosols exist? Understanding aerosol lifetimes using the two-dimensional volatility basis set, *Environ. Chem.*, 10, 151–157, 2013.
- Ehn, M., Thornton, J. A., Kleist, E., Sipilä, M., Junninen, H., Pullinen, I., Springer, M., Rubach, F., Tillmann, R., Lee, B., Lopez-Hilfiker, F., Andres, S., Acir, I.-H., Rissanen, M., Jokinen, T., Schobesberger, S., Kangasluoma, J.,

Kontkanen, J., Nieminen, T., Kurtén, T., Nielsen, L. B., Jørgensen, S., Kjaergaard, H. G., Canagaratna, M., Maso, M. D., Berndt, T., Petäjä, T., Wahner, A., Kerminen, V.-M., Kulmala, M., Worsnop, D. R., Wildt, J. and Mentel, T. F.: A large source of low-volatility secondary organic aerosol. *Nature* 506, 476–479, 2014.

Environ: User's guide to the comprehensive air quality model with extensions (CAMx), version 4.02, report, ENVIRON Int. Corp., Novato, Calif., available at: <http://www.camx.com> (last access: 8 January 2021), 2003.

Feng, Y., Ramanathan, V., and Kotamarthi, V. R.: Brown carbon: a significant atmospheric absorber of solar radiation? *Atmos. Chem. Phys.*, 13, 8607–8621, <https://doi.org/10.5194/acp-13-8607-2013>, 2013.

Forrister, H., Liu, J., Scheuer, E., Dibb, J., Ziemba, L., Thornhill, K. L., Anderson, B., Diskin, G., Perring, A. E., and Schwarz, J. P.: Evolution of brown carbon in wildfire plumes, *Geophys. Res. Lett.*, 42, 4623–4630, <https://doi.org/10.1002/2015GL063897>, 2015.

Fountoukis, C. and Nenes, A.: ISORROPIA II: a computationally efficient thermodynamic equilibrium model for K^+ - Ca^{2+} - Mg^{2+} - NH_4^+ - Na^+ - SO_4^{2-} - NO_3^- - Cl^- - H_2O aerosols, *Atmos. Chem. Phys.*, 7, 4639–4659, 2007.

Fountoukis, C., Nenes, A., Sullivan, A., Weber, R., Van Reken, T., Fischer, M., Matias, E., Moya, M., Farmer, D. and Cohen, R. C.: Thermodynamic characterization of Mexico City aerosol during MILAGRO 2006, *Atmos. Chem. Phys.*, 9, 2141–2156, 2009.

Fountoukis, C., Racherla, P. N., Denier Van Der Gon, H. A. C., Polymeneas, P., Charalampidis, P. E., Pilinis, C., Wiedensohler, A., Dall'Osto, M., O'Dowd, C. and Pandis, S. N.: Evaluation of a three-dimensional chemical transport model (PMCAMx) in the European domain during the EUCAARI May 2008 campaign, *Atmos. Chem. Phys.*, 11, 10331–10347, 2011.

Gonçalves-Ageitos, M., Dawson, M., Obiso, V., Klose, M., Jorba, O., Balkanski, Y., Perlwitz, J., Miller, R., Pérez García-Pando, et al. Dust mineralogy in the Multiscale Online Non-hydrostatic Atmosphere Chemistry Model. *Geoscientific Model Development*, in prep.

Guenther, A., Karl, T., Harley, P., Wiedinmyer, C., Palmer, P. I. and Geron, C.: Estimates of global terrestrial isoprene emissions using MEGAN (Model of Emissions of Gases and Aerosols from Nature), *Atmos. Chem. Phys.*, 6, 3181–3210, 2006.

Guo, H., Xu, L., Bougiatioti, A., Cerully, K. M., Capps, S. L., Hite Jr., J. R., Carlton, A. G., Lee, S.-H., Bergin, M. H., Ng, N. L., Nenes, A., and Weber, R. J.: Fine-particle water and pH in the southeastern United States, *Atmos. Chem. Phys.*, 15, 5211–5228, 2015.

Hazeleger, W., et al.: EC-Earth V2.2: Description and validation of a new seamless earth system prediction model, *Clim. Dyn.*, 39, 2611–2629, 2011.

Heitzenberg, J.: Fine particles in the global troposphere: a review, *Tellus*, 41B, 149–160, 1989.

Haustein, K., Pérez, C., Baldasano, J. M., Jorba, O., Basart, S., Miller, R. L., Janjic, Z., Black, T., Nickovic, S., Todd, M. C., Washington, R., Müller, D., Tesche, M., Weinzierl, B., Esselborn, M., and Schladitz, A.: Atmospheric dust modeling from meso to global scales 215 with the online NMMB/BSC-Dust model - Part 2: Experimental campaigns in Northern Africa, *Atmospheric Chemistry and Physics*, 12, 2933–2958, <https://doi.org/10.5194/acp-12-2933-2012>, 2012.

Holben, B. N., Eck, T. F., Slutsker, I., Tanré, D., Buis, J. P., Setzer, A., Vermote, E., Reagan, J. A., Kaufman, Y. J., Nakajima, T., Lavenu, F., Jankowiak, I., and Smirnov, A.: AERONET-A federated instrument network and data archive for aerosol characterization, *Remote Sensing of Environment*, 66, 1–16, 1998.

Iversen, T., Bentsen, M., Bethke, I., Debernard, J. B., Kirkevåg, A., Seland, Ø., Drange, H., Kristjansson, J. E., Medhaug, I., Sand, M., and Seierstad, I. A.: The Norwegian Earth System Model, NorESM1-M – Part 2: Climate response and scenario projections, *Geosci. Model Dev.*, 6, 389–415, 2013.

Jacob, D. J.: Heterogeneous chemistry and tropospheric ozone, *Atmos. Environ.*, 34, 2131–2159, 2000.

Jacobson, M. Z., Tabazadeh, A. and Turco, R. P.: Simulating equilibrium within aerosols and nonequilibrium between gases and aerosols, *J. Geophys. Res.*, 101, 9079–9091, 1996.

- Jacobson, M. Z.: Chemical Equilibrium and dissolution processes, *Fundamentals of Atmospheric Modeling*, Cambridge University Press, New York, pp. 476–510, (Chapter 18), 1999a.
- Jacobson, M. Z.: Studying the effect of calcium and magnesium on size-distributed nitrate and ammonium with EQUISOLV II, *Atmos. Environ.*, 33, 3635–3649, 1999b.
- Jathar, S.H., Mahmud, A., Barsanti, K.C., Asher, W.E., Pankow, J.F., Kleeman, M.J.: Water uptake by organic aerosol and its influence on gas/particle partitioning of secondary organic aerosol in the United States. *Atmos. Environ.* 129, 142–154, 2016.
- Jin, X., Wang, Y., Li, Z., Zhang, F., Xu, W., Sun, Y., Fan, X., Chen, G., Wu, H., Ren, J., Wang, Q., and Cribb, M.: Significant contribution of organics to aerosol liquid water content in winter in Beijing, China, *Atmos. Chem. Phys.*, 20, 901–914, 2020.
- Jo, D. S., Park, R. J., Lee, S., Kim, S.-W., and Zhang, X.: A global simulation of brown carbon: implications for photochemistry and direct radiative effect, *Atmos. Chem. Phys.*, 16, 3413–3432, <https://doi.org/10.5194/acp-16-3413-2016>, 2016.
- Jo, D. S., Park, R. J., Kim, M. J., and Spracklen, D. V.: Effects of chemical aging on global secondary organic aerosol using the volatility basis set approach, *Atmos. Environ.*, 81, 230–244, 2013.
- Jöckel, P., Tost, H., Pozzer, A., Bruehl, C., Buchholz, J., Ganzeveld, L., Hoor, P., Kerkweg, A., Lawrence, M. G., Sander, R., Steil, B., Stiller, G., Tanarhte, M., Taraborrelli, D., Van Aardenne, J., and Lelieveld, J.: The atmospheric chemistry general circulation model ECHAM5/MESSy1: consistent simulation of ozone from the surface to the mesosphere, *Atmos. Chem. Phys.*, 6, 5067–5104, 2006.
- Jokinen, T., Berndt, T., Makkonen, R., Kerminen, V.-M., Junninen, H., Paasonen, P., Stratmann, F., Herrmann, H., Guenther, A. B., Worsnop, D. R., Kulmala, M., Ehn, M., and Sipilä, M.: Production of extremely low volatile organic compounds from biogenic emissions: Measured yields and atmospheric implications. *PNAS* 112, 7123–7128, 2015.
- Jorba, O., Dabdub, D., Blaszcak-Boxe, C., Pérez, C., Janjic, Z., Baldasano, J. M., Spada, M., Badia, A., and Gonçalves, M.: Potential significance of photoexcited NO₂ on global air quality with the NMMB/BSC chemical transport model, *Journal of Geophysical Research*, 117, D13 301, <https://doi.org/10.1029/2012JD017730>, <http://dx.doi.org/10.1029/2012JD017730>, 2012
- Journet, E., Balkanski, Y., and Harrison, S. P.: A new data set of soil mineralogy for dust-cycle modeling, *Atmospheric Chemistry and Physics*, 14, 3801–3816, <https://doi.org/10.5194/acp-14-3801-2014>, <http://www.atmos-chem-phys.net/14/3801/2014/>, 2014.
- Kakavas, S. and Pandis, S. N.: Effects of urban dust emissions on fine and coarse PM levels and composition, *Atmos. Environ.*, 246, 118006, 2021.
- Kane, S. M., Caloz, F. and Leu M. T.: Heterogeneous uptake of gaseous N₂O₅ by (NH₄)₂SO₄, NH₄HSO₄, and H₂SO₄ aerosols, *J. Phys. Chem. A*, 105, 6465– 6470, 2001.
- Karl, M., Tsigaridis, K., Vignati, E., and Dentener, F.: Formation of secondary organic aerosol from isoprene oxidation over Europe, *Atmos. Chem. Phys.*, 9, 7003–7030, 2009.
- Karydis, V. A., Tsimpidi, A. P., Pozzer, A., Astitha, M., Lelieveld J.: Effects of mineral dust on global atmospheric nitrate concentrations, *Atmos. Chem. Phys.*, 16, 1491–1509, 2016.
- Kerminen, V.-M., Chen, X., Vakkari, V., Petäjä, T., Kulmala, M., and Bianchi, F.: Atmospheric new particle formation and growth: review of field observations. *Environ. Res. Lett.* 13, 103003, 2018.
- Kim, Y. P., Seinfeld, J. H., and Saxena, P.: Atmospheric gas – aerosol equilibrium I. Thermodynamic model, *Aerosol Sci. Technol.*, 19, 157–181, 1993a.
- Kim, Y. P., Seinfeld, J. H., and Saxena, P.: Atmospheric gas – aerosol equilibrium II. Analysis of common approximations and activity coefficient calculation methods, *Aerosol Sci. Technol.*, 19, 182–198, 1993b.
- Kim, Y. P. and Seinfeld, J. H.: Atmospheric gas – aerosol equilibrium III. Thermodynamics of crustal elements Ca²⁺, K⁺, and Mg²⁺, *Aerosol Sci. Technol.*, 22, 93–110, 1995.

Kirkevåg, A., Iversen, T., Seland, Ø., Hoose, C., Kristjánsson, J. E., Struthers, H., Ekman, A. M. L., Ghan, S., Griesfeller, J., Nilsson, E. D., and Schulz, M.: Aerosol–climate interactions in the Norwegian Earth System Model – NorESM1-M, *Geosci. Model Dev.*, 6, 207–244, 2013.

Klose, M., Jorba, O., Gonçalves Ageitos, M., Escribano, J., Dawson, M. L., Obiso, V., Di Tomaso, E., Basart, S., Montané Pinto, G., Macchia, F., Ginoux, P., Guerschman, J., Prigent, C., Huang, Y., Kok, J., Miller, R. L., and Pérez García Pando, C.: Mineral dust cycle in the Multiscale Online Nonhydrostatic Atmosphere Chemistry model (MONARCH) Version 2.0, *Geoscientific Model Development*, in prep.

Kok, J. F.: Does the size distribution of mineral dust aerosols depend on the wind speed at emission? *Atmospheric Chemistry and Physics*, 11, 10 149–10 156, <https://doi.org/10.5194/acp-11-10149-2011>, 2011.

Koo B., Metzger S., Vennam P., Emery C., Wilson G., and Yarwood G.: Comparing the ISORROPIA and EQSAM Aerosol Thermodynamic Options in CAMx, In: Mensink C., Gong W., Hakami A. (eds) *Air Pollution Modeling and its Application XXVI. ITM 2018. Springer Proceedings in Complexity*. Springer, Cham. https://doi.org/10.1007/978-3-030-22055-6_16, 2020.

Kulmala, M., Asmi, A., Lappalainen, H. K., Carslaw, K. S., Poschl, U., Baltensperger, U., Hov, Ø., Brenquier, J.-L., Pandis, S. N., Facchini, M. C., Hansson, H.-C., Wiedensohler, A., and O'Dowd, C. D.: Introduction: European Integrated Project on Aerosol Cloud Climate and Air Quality interactions (EUCAARI) – integrating aerosol research from nano to global scales, *Atmos. Chem. Phys.*, 9, 2825–2841, 2009.

Kulmala, M., Petäjä, T., Nieminen, T., Sipilä, M., Manninen, H. E., Lehtipalo, K., Dal Maso, M., Aalto, P. P., Junninen, H., Paasonen, P., Riipinen, I., Lehtinen, K. E. J., Laaksonen, A. and Kerminen, V.-M.: Measurement of the nucleation of atmospheric aerosol particles. *Nat. Protocols* 7, 1651–1667, 2012.

Kusik, C. and Meissner, H.: Electrolyte activity coefficients in inorganic processing, *AIChE Sym. S.*, 74, 14–20, 1978.

Laskin, A., Laskin, J., and Nizkorodov, S. A.: Chemistry of atmospheric brown carbon, *Chem. Rev.*, 115, 4335–4382, <https://doi.org/10.1021/cr5006167>, 2015.

Li, J., Carlson, B. E., Dubovik, O., and Lacis, A. A.: Recent trends in aerosol optical properties derived from AERONET measurements, *Atmospheric Chemistry and Physics*, 14, 12 271–12 289, 2014.

Lin, G., J. E. Penner, M. G. Flanner, S. Sillman, L. Xu, and C. Zhou (2014), Radiative forcing of organic aerosol in the atmosphere and on snow: Effects of SOA and brown carbon, *J. Geophys. Res. Atmos.*, 119, 7453–7476, [doi:10.1002/2013JD021186](https://doi.org/10.1002/2013JD021186).

Liu, J., Bergin, M., Guo, H., King, L., Kotra, N., Edgerton, E., and Weber, R. J.: Size-resolved measurements of brown carbon in water and methanol extracts and estimates of their contribution to ambient fine-particle light absorption, *Atmos. Chem. Phys.*, 13, 12389–12404, <https://doi.org/10.5194/acp-13-12389-2013>, 2013.

Meng, Z. Y., Seinfeld, J. H., Saxena, P., and Kim, Y. P.: Atmospheric gas – aerosol equilibrium IV. Thermodynamics of carbonates, *Aerosol Sci. Technol.*, 23, 131–154, 1995.

Meng, Z. Y., and Seinfeld, J. H.: Time scales to achieve atmospheric gas-aerosol equilibrium for volatile species, *Atmospheric Environment*, 30, 2889–2900, [10.1016/1352-2310\(95\)00493-9](https://doi.org/10.1016/1352-2310(95)00493-9), 1996.

Metzger, S., Dentener, F., Pandis, S., and Lelieveld, J.: Gas/aerosol partitioning: 1. A computationally efficient model, *J. Geophys. Res.*, 107, 4312, [doi:10.1029/2001JD001102](https://doi.org/10.1029/2001JD001102), 2002a.

Metzger, S., Dentener, F., Krol, M., Jeuken, A., and Lelieveld, J.: Gas/aerosol partitioning: 2. Global modeling results, *J. Geophys. Res.*, 107, 4313, [doi:10.1029/2001JD001103](https://doi.org/10.1029/2001JD001103), 2002b.

Metzger, S., Mihalopoulos, N., and Lelieveld, J.: Importance of mineral cations and organics in gas-aerosol partitioning of reactive nitrogen compounds: case study based on MINOS results, *Atmos. Chem. Phys.*, 6, 2549–2567, 2006.

Metzger, S., Steil, B., Abdelkader, M., Klingmüller, K., Xu, L., Penner, J. E., Fountoukis, C., Nenes, A., and Lelieveld, J.: Aerosol water parameterisation: a single parameter framework, *Atmos. Chem. Phys.*, 16, 7213–7237, 2016.

- Moya, M., Fountoukis, C., Nenes, A., Matias, E., and Grutter, M.: Predicting diurnal variability of fine inorganic aerosols and their gas-phase precursors near downtown Mexico City, *Atmos. Chem. Phys.*, 7, 11257–11294, 2007.
- Murphy, B. N., Donahue, N. M., Fountoukis, C., Dall'Osto, M., O'Dowd, C., Kiendler-Scharr, A., and Pandis, S. N.: Functionalization and fragmentation during ambient organic aerosol aging: application of the 2-D volatility basis set to field studies, *Atmospheric Chemistry and Physics*, 12, 10797–10816, 10.5194/acp-12-10797-2012, 2012.
- Nenes, A., Pandis, S. N., Pilinis, C.: ISORROPIA: A new thermodynamic equilibrium model for multiphase multicomponent inorganic aerosols, *Aquat. Geochem.*, 4, 123–152, 1998.
- Nenes, A., Pilinis, C., and Pandis, S. N.: Continued development and testing of a new thermodynamic aerosol module for urban and regional air quality models, *Atmos. Environ.*, 33, 1553–1560, 1999.
- Ng, N. L., Kroll, J. H., Keywood, M. D., Bahreini, R., Varutbangkul, V., Flagan, R. C., Seinfeld, J. H., Lee, A., and Goldstein, A. H.: Contribution of first- versus second-generation products to secondary organic aerosols formed in the oxidation of biogenic hydrocarbons, *Environ. Sci. Technol.*, 40, 2283–2297, 2006.
- Nickovic, S., Vukovic, A., Vujadinovic, M., Djurdjevic, V., and Pejanovic, G.: Technical Note: High-resolution mineralogical database of dust-productive soils for atmospheric dust modeling, *Atmospheric Chemistry and Physics*, 12, 845–855, <https://doi.org/10.5194/acp-12-255-2012>, 2012.
- O'Dowd, C. D., Langmann, B., Varghese, S., Scannell, C., Ceburnis, D. and Facchini, M. C.: A combined organic-inorganic sea-spray source function, *Geophys. Res. Lett.*, 35, L01801, 2008.
- Pandis, S. N., Wexler, A. S., and Seinfeld, J. H.: Secondary organic aerosol formation and transport. 2. Predicting the ambient secondary organic aerosol-size distribution, *Atmos. Environ. A-Gen.*, 27, 2403–2416, 1993.
- Pankow, J. F.: An absorption-model of gas-particle partitioning of organic-compounds in the atmosphere, *Atmos. Environ.*, 28, 185–188, 1994.
- Park, R. J., Kim, M. J., Jeong, J. I., Youn, D., and Kim, S. (2010). A contribution of brown carbon aerosol to the aerosol light absorption and its radiative forcing in east Asia. *Atmospheric Environment*, 44:1414–1421.
- Pathak, R. K., Presto, A. A., Lane, T. E., Stanier, C. O., Donahue, N. M., and Pandis, S. N.: Ozonolysis of alpha-pinene: parameterization of secondary organic aerosol mass fraction, *Atmospheric Chemistry and Physics*, 7, 3811–3821, 2007.
- Pérez, C., Haustein, K., Janjic, Z., Jorba, O., Huneus, N., Baldasano, J. M., Black, T., Basart, S., Nickovic, S., Miller, R. L., Perlwitz, J. P., Schulz, M., and Thomson, M.: Atmospheric dust modeling from meso to global scales with the online NMMB/BSCDust model; Part 1: Model description, annual simulations and evaluation, *Atmospheric Chemistry and Physics*, 11, 13 001–13 027, <https://doi.org/10.5194/acp-11-13001-2011>, 2011.
- Perlwitz, J. P., Pérez García-Pando, C., and Miller, R. L.: Predicting the mineral composition of dust aerosols - Part 1: Representing key processes, *Atmospheric Chemistry and Physics*, 15, 11 593–11 627, <https://doi.org/10.5194/acp-15-11593-2015>, 2015a
- Perlwitz, J. P., Pérez García-Pando, C., and Miller, R. L.: Predicting the mineral composition of dust aerosols - Part 2: Model evaluation and identification of key processes with observations, *Atmospheric Chemistry and Physics*, 15, 11 629–11 652, <https://doi.org/10.5194/acp15-11629-2015>, 2015b.
- Petters, M. D. and Kreidenweis, S. M.: A single parameter representation of hygroscopic growth and cloud condensation nucleus activity, *Atmos. Chem. Phys.*, 7, 1961–1971, 2007.
- Pierce, J. R. and Adams, P. J. (2007) Efficiency of cloud condensation nuclei formation from ultrafine particles. *Atmos. Chem. Phys.*, 7, ISI:000244712400004.
- Pierce J. R., G. Theodoritsi, P. J. Adams, and S. N. Pandis (2009) Parameterization of the effect of sub-grid scale aerosol dynamics on aerosol number emission rates, *J. Aerosol Science*, 40, 385–393.
- Pilinis, C., Capaldo, K. P., Nenes, A., and Pandis, S. N.: MADM– a new multicomponent aerosol dynamics

model, *Aerosol Sci. Tech.*, 32, 482–502, 2000.

Pringle, K. J., Tost, H., Message, S., Steil, B., Giannadaki, D., Nenes, A., Fountoukis, C., Stier, P., Vignati, E., and Lelieveld, J.: Description and evaluation of GMX: a new aerosol submodel for global simulations (v1), *Geoscientific Model Development*, 3, 391–412, 2010.

Pugh, T. A. M., MacKenzie, A. R., Hewitt, C. N., Langford, B., Edwards, P. M., Furneaux, K. L., Heard, D. E., Hopkins, J. R., Jones, C. E., Karunaharan, A., Lee, J., Mills, G., Misztal, P., Moller, S., Monks, P. S., and Whalley, L. K.: Simulating atmospheric composition over a South-East Asian tropical rainforest: performance of a chemistry box model, *Atmos. Chem. Phys.*, 10, 279–298, 2010.

Pye, H. O. T., Nenes, A., Alexander, B., Ault, A. P., Barth, M. C., Clegg, S. L., Collett Jr., J. L., Fahey, K. M., Hennigan, C. J., Herrmann, H., Kanakidou, M., Kelly, J. T., Ku, I.-T., McNeill, V. F., Riemer, N., Schaefer, T., Shi, G., Tilgner, A., Walker, J. T., Wang, T., Weber, R., Xing, J., Zaveri, R. A., and Zuend, A.: The Acidity of Atmospheric Particles and Clouds, *Atmos. Chem. Phys.*, 20, 4809–4888, 2020.

Roeckner, E., et al.: The Atmospheric General Circulation Model ECHAM5. Part I: Model Description. MPI Report 349, Max Planck Institute for Meteorology, Hamburg, Germany, 127 pp, 2003.

Saleh, R., Robinson, E. S., Tkacik, D. S., Ahern, A. T., Liu, S., Aiken, A. C., Sullivan, R. C., Presto, A. A., Dubey, M. K., Yokelson, R. J., et al. (2014). Brownness of organics in aerosols from biomass burning linked to their black carbon content. *Nature Geoscience*, 7:647–650.

Saleh, R., Marks, M., Heo, J., Adams, P. J., Donahue, N. M., and Robinson, A. L. (2015). Contribution of brown carbon and lensing to the direct radiative effect of carbonaceous aerosols from biomass and biofuel burning emissions. *Journal of Geophysical Research: Atmospheres*, 120:10–285.

San Martini, F. M.: Decision Support Tools for Urban Air Quality Management, Ph.D Thesis, Massachusetts Institute of Technology, p. 283, 2004.

Schuster, G. L., et al Remote sensing of soot carbon - Part 1: Distinguishing different absorbing aerosol species, *Atmos. Chem. Phys.*, 16, 1565–1585, 2016.

Seinfeld, J. H. and Pandis, S. N.: Atmospheric Chemistry and Physics: from Air Pollution to Climate Change 2nd Edn., John Wiley & Sons, Inc., Hoboken, New Jersey, 2006.

Skamarock, W. C., Klemp, J. B., Dudhia, J., Gill, D. O., Barker, D. M., Duda, M. G., Huang, X., Wang, W., Powers, J. G.: A Description of the Advanced Research WRF Version 3, NCAR Technical Note, available at: <https://opensky.ucar.edu/islandora/object/technotes%3A500/datastream/PDF/view> (last access: 3 February 2021), 2008.

Song, S., Gao, M., Xu, W., Shao, J., Shi, G., Wang, S., Wang, Y., Sun, Y., and McElroy, M. B.: Fine-particle pH for Beijing winter haze as inferred from different thermodynamic equilibrium models, *Atmos. Chem. Phys.*, 18, 7423–7438, 2018.

Strader, R., Lurmann, F., and Pandis, S. N.: Evaluation of secondary organic aerosol formation in winter, *Atmos. Environ.*, 33, 4849–4863, 1999.

Tasoglou, A., Louvaris, E., Florou, K., Liangou, A., Karnezi, E., Kaltsonoudis, C., Wang, N., and Pandis, S. N.: Aerosol light absorption and the role of extremely low volatility organic compounds, *Atmos. Chem. Phys.*, 20, 11625–11637, <https://doi.org/10.5194/acp-20-11625-2020>, 2020.

Toon, O. B., Maring, H., Dibb, J., Ferrare, R., Jacob, D. J., Jensen, E. J., and Rosenlof, K. H.: Planning, implementation, and scientific goals of the Studies of Emissions and Atmospheric Composition, Clouds and Climate Coupling by Regional Surveys (SEAC4RS) field mission, *J. Geophys. Res.-Atmos.*, 121, 4967–5009, <https://doi.org/10.1002/2015JD024297>, 2016.

Tsigaridis, K., Kanakidou, M.: The present and future of secondary organic aerosol direct forcing on climate, *Current Climate Change Reports*, <https://doi.org/10.1007/s40641-018-0092-3>, 2018.

Tsimpidi, A. P., Karydis, V. A., and Pandis, S. N.: Response of fine particulate matter to emission changes of oxides of nitrogen and anthropogenic volatile organic compounds in the Eastern United States, *J. Air Waste Manage. Assoc.*, 58, 1463–1473, [10.3155/1047-3289.58.11.1463](https://doi.org/10.3155/1047-3289.58.11.1463), 2008.

- Tsimpidi, A. P., Karydis, V. A., Pozzer, A., Pandis, S. N., and Lelieveld, J.: ORACLE (v1.0): module to simulate the organic aerosol composition and evolution in the atmosphere, *Geoscientific Model Development*, 7, 3153–3172, 10.5194/gmd-7-3153-2014, 2014.
- Tsimpidi, A. P., Karydis, V. A., Pandis, S. N., and Lelieveld, J.: Global combustion sources of organic aerosols: model comparison with 84 AMS factor-analysis data sets, *Atmos. Chem. Phys.*, 16, 8939–8962, 10.5194/acp-16-8939-2016, 2016.
- Vignati, E., Wilson, J., and Stier, P.: M7: An efficient size-resolved aerosol microphysics module for large-scale aerosol transport models, *J. Geophys. Res.*, 109, 10.1029/2003jd004485, 2004.
- Visschedijk, A. J. H., Zandveld, P. and Denier van der Gon, H. A. C.: TNO Report 2007 A-R0233/B: A high resolution gridded European emission database for the EU integrated project GEMS, Netherlands, Organization for Applied Scientific Research, 2007.
- Wang, X., Heald, C. L., Ridley, D. A., Schwarz, J. P., Spackman, J. R., Perring, A. E., Coe, H., Liu, D., and Clarke, A. D.: Exploiting simultaneous observational constraints on mass and absorption to estimate the global direct radiative forcing of black carbon and brown carbon, *Atmos. Chem. Phys.*, 14, 10989–11010, <https://doi.org/10.5194/acp-14-10989-2014>, 2014.
- Wang, X., Heald, C. L., Liu, J., Weber, R. J., Campuzano-Jost, P., Jimenez, J. L., Schwarz, J. P., and Perring, A. E.: Exploring the observational constraints on the simulation of brown carbon, *Atmos. Chem. Phys.*, 18, 635–653, <https://doi.org/10.5194/acp-18-635-2018>, 2018.
- Wexler, A. S. and Clegg, S. L.: Atmospheric aerosol models for systems including the ions H^+ , NH_4^+ , Na^+ , SO_4^{2-} , NO_3^- , Cl^- , Br^- , and H_2O , *J. Geophys. Res.*, 107, 4207, doi:10.1029/2001JD000451, 2002.
- Wong, J. P. S., Tsagkaraki, M., Tsiodra, I., Mihalopoulos, N., Violaki, K., Kanakidou, M., Sciare, J., Nenes, A., and Weber, R. J.: Atmospheric evolution of molecular-weight-separated brown carbon from biomass burning, *Atmos. Chem. Phys.*, 19, 7319–7334, 2019.
- Zeng et al.: Global Measurements of brown carbon and estimated direct radiative effects, *Geophys. Res. Lett.*, 47, agupubs.onlinelibrary.wiley.com/doi/epdf/10.1029/2020GL088747, 2020.
- Zhang, Y., Forrister, H., Liu, J., Dibb, J., Anderson, B., Schwarz, J.P., Perring, A.E., Jimenez, J.L., Campuzano-Jost, P., Wang, Y., Nenes, A., Weber, R.J. Convection transports brown carbon to the upper troposphere affecting top of atmosphere radiative forcing, *Nature Geosci.*, doi:10.1038/ngeo2960, 2017.
- Zhang, A., Wang, Y., Zhang, Y., Weber, R. J., Song, Y., Ke, Z., and Zou, Y.: Modeling the global radiative effect of brown carbon: a potentially larger heating source in the tropical free troposphere than black carbon, *Atmos. Chem. Phys.*, 20, 1901–1920, 2020.